Energy barriers in patterned media

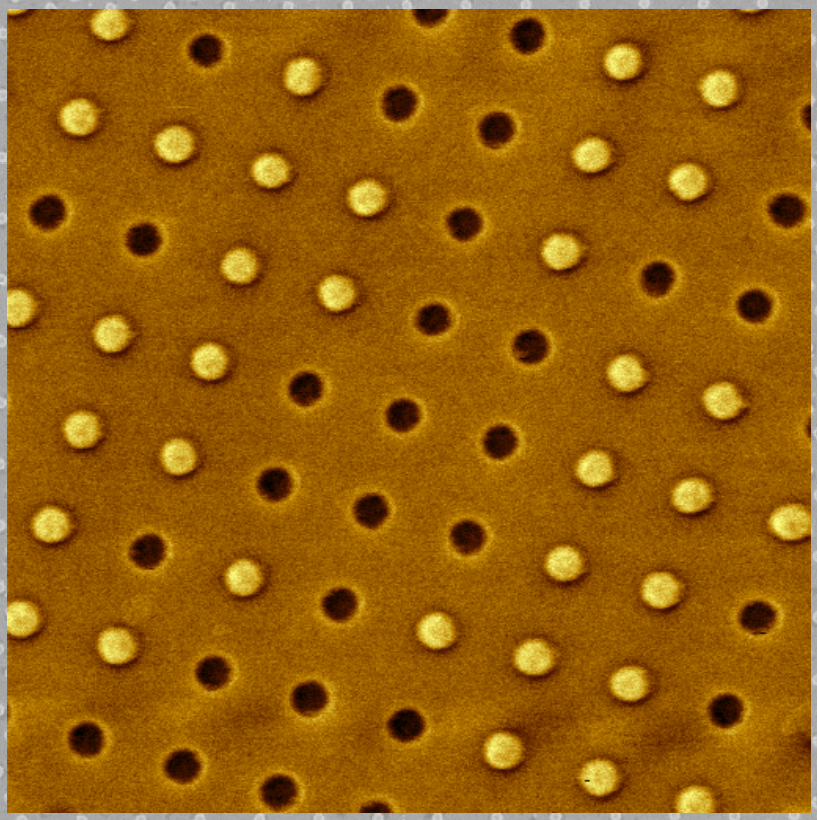

Jeroen de Vries

Graduation committee

Prof. dr. ir. Ton J. Mouthaan	University of Twente (chairman and secretary)
Prof. dr. Miko C. Elwenspoek	University of Twente (promotor)
Prof. dr. ir. Leon Abelmann	University of Twente (assistant promotor)
Dr. Nobuaki Kikuchi	Tohoku University, Japan
Prof. dr. Andreas Manz	KIST Europe, Germany
Prof. dr. ir. Bene Poelsema	University of Twente
Prof. dr. Thomas Thomson	Manchester University, United Kingdom
Prof. dr. ir. Wilfred G. van der Wiel	University of Twente

Paranymphs

Maaike Elzinga
Michel Franken

UNIVERSITY OF TWENTE.

The research presented in this dissertation was carried out at the Transducers Science & Technology group at the MESA$^+$ Institute for Nanotechnology at the University of Twente, Enschede, the Netherlands. This research is supported by the Dutch Technology Foundation STW, which is part of the Netherlands Organisation for Scientific Research (NWO) and partly funded by the Ministry of Economic Affairs (project number 10013). The research was part of the "Thin Film Nanomanufacturing" project. ("Ataktos – The origins of switching field distribution in patterned magnetic multilayered media", project number 10013)

Cover design by Jeroen de Vries. On the front a scanning electron microscopy image of a patterned media sample with in front of it a magnetic force microscopy image of patterned media sample. On the back a Hall cross structure with the patterned magnetic islands.

Printed by Gildeprint Drukkerijen, Enschede, the Netherlands

Electronic mail address: j.devries-5@alumnus.utwente.nl
ISBN 978-90-365-0640-3
DOI 10.3990/1.9789036506403

ENERGY BARRIERS IN PATTERNED MEDIA

DISSERTATION

to obtain
the degree of doctor at the University of Twente,
on the authority of the rector magnificus,
prof. dr. H. Brinksma,
on account of the decision of the graduation committee,
to be publicly defended
on Thursday, 17 October 2013 at 14:45

by

Jeroen de Vries

born on January 5 1982,
in Stede Broec, the Netherlands

This dissertation is approved by

Prof. dr. Miko C. Elwenspoek	University of Twente (promotor)
Prof. dr. ir. Leon Abelmann	University of Twente (assistant promotor)

Contents

Chapter 1

Introduction

1.1 Magnetic data storage

For thousands of years humankind has tried to preserve information. From engravings in marble slabs to current hard disk technology, information has been kept available for future usage.

To ensure that information can be stored at all, the data needs to be retained in a certain meta-stable state, which is distinguishable from the other states or the environment. For the engravings in marble, information is stored in the height difference and the energy barrier is caused by the attractive force between the atoms. For the magnetic hard disk, the data is the difference in the orientations of the magnetisation and the energy barrier is due to the magnetic anisotropy. In both cases the information is separated from the non-information by an energy barrier.

In magnetic data storage this energy barrier can be overcome by a magnetic writing field in order to change the magnetisation direction. The stored data however, will not stay in this state indefinitely. Given sufficient time and under influence of thermal activation, the chances of overcoming the energy barrier increase.

This means that the energy barrier needs to be sufficiently high to store information on a hard disk and keep the information for at least 10 years, which is the acceptable storage time for hard disks (Qin et al., 2009). This energy barrier is directly related to the storage density as the height of the energy barrier is the product of the magnetic anisotropy and the magnetic volume.

The amount of storage capacity has increased tremendously since the capability of storing digital information. In 1956 the first commercial hard disks became available, which were capable of storing 5 MB on fifty 24" disks. At the time of writing this introduction, hard disks are on the market that are able to store 4 TB on four 3.5"disks. Although this increase in capacity is enormous, it is expected that we will require even more storage capacity in the future.

In current hard disk technology the information is stored on a continuous

granular film. A bit is stored in several hundreds of these grains (Terris and Thomson, 2005) and the increase in data density is achieved in a large part by decreasing the grain size. This decrease in grain size however, lowers the energy barrier which separates the magnetic states due to the decrease in magnetic volume, down to a point where the state is no longer thermally stable at room temperature. This point is known as the superparamagnetic limit (Moser et al., 2002).

To be able to increase the areal bit density while avoiding the superparamagnetic limit, a high anisotropy material can be used to counteract the decrease in energy barrier height caused by a decrease in magnetic volume. This high anisotropy material would make it possible to decrease the grain size even further while maintaining a sufficiently high signal-to-noise ratio (SNR). The increase in anisotropy however, results in a higher write field. Since the write field of magnetic recording heads is limited, at one point the medium becomes unwritable. These problems (stability, SNR and writability) form a trilemma and solutions which keep a high SNR while ensuring thermal stability and which can be written by a magnetic head, need to be found (Qin et al., 2009).

Several solutions are suggested which make it possible to keep increasing the areal bit density while postponing the superparamagnetic limit and taking into account the trilemma. One of these solutions is the use of heat assisted magnetic recording or HAMR (Kryder et al., 2008). To write data using HAMR, a high anisotropy medium is locally heated to decrease the coercivity below that of the applied magnetic write pulse. This makes it possible for the bits to still be thermally stable at room temperature while ensuring the writability of the medium. Currently already a successful test of 1 Tbit/in^2 has been performed (Wu et al., 2013) and eventually storage densities of over 5 Tbit/in^2 might be achieved (Wang et al., 2013).

A different solution is microwave assisted magnetic recording or MAMR (Zhu et al., 2008). In MAMR a localised, high frequency field is applied to the medium, as in ferromagnetic resonance. The AC field increases the precession of the magnetisation, which reduces the field required to reverse the magnetisation direction to the state parallel to the direction of the applied magnetic field.

Another solution which might be combined in the future with either HAMR or MAMR, is magnetic bit patterned media. In bit patterned media the disk no longer consists of a continuous granular magnetic film, but of a pre-patterned disk with fixed bit positions, separated by non-magnetic material. In granular media, the bit boundary is determined by the grain boundary but in patterned media it is determined by the patterning process. This makes it possible to use a single or a small number of strongly coupled grains to store a single bit of information. These well defined islands ensure a high SNR and stability of the stored information while still being writable by a magnetic head.

The patterned media however suffer from a variation in required writing field from island to island, known as the switching field distribution (SFD). Due to the SFD a high anisotropy island (strong island) requires a larger magnetic

field than a low anisotropy island (weak island). This might cause a neighbouring low anisotropy island to be accidentally written by the stray field from the write head, when a high anisotropy island is written. This results in data loss and the SFD needs to be reduced before bit patterned media can be used in commercial products. There is strong evidence that this variation in required switching field is caused by variations in anisotropy which are already present in the film before patterning (Lau et al., 2008; Thomson et al., 2006).

Besides this switching field distribution between the various islands, there is also a distribution in switching field required for the reversal of a single island. This distribution is caused by thermal activation, which lowers the energy barrier. Due to the statistical nature of the thermal activation, there is a slight variation in the field at which the island reverses if the field is slowly ramped up. This thermal switching field distribution occurs when the magnetic reversal takes place at temperatures above 0 K (Engelen et al., 2010).

Analysis of the thermal switching field distribution allows us to extract the energy barrier of a single island in the absence of an external field as well as the switching field in the absence of thermal fluctuations. Variations in these energy barriers results in the large SFD between the islands.

When a magnetic field is applied to the patterned media it usually results in complete reversal of an island when the energy barrier is overcome. In chapter 2 the pinning of a domain wall in a 350 nm island is investigated, indicating multiple energy barriers in a single island which only become visible when the field is applied under a large angle with the magnetic easy axis.

Investigation of the difference between the switching field in the absence of thermal fluctuations and the energy barrier in the absence of an external field gives more insight in the SFD. In chapter 3 the energy barrier in the absence of an external field and the switching field in the absence of thermal fluctuations are investigated for two multilayer films and an alloy. Finally chapter 4 deals with the temperature dependence of the mentioned energy barriers and switching fields caused by temperature dependent variation in magnetic material parameters.

1.2 Long term data storage

Given sufficient time, energy barriers will be overcome by thermal activation or degradation of the medium, resulting in data loss. The time it takes to overcome the energy barrier is highly dependent on the height of the energy barrier and environmental influences which aid in overcoming the energy barrier. One such influence is an elevated temperature which lowers the energy barrier, while simultaneously increasing the chance of overcoming the energy barrier.

The energy barrier in current hard disk technology is chosen to ensure a data stability for at least 10 years (Qin et al., 2009). This means that a hard disk left for a (much) longer time will not be readable anymore, even if the data

format in which the information is stored is still supported. The focus of the hard disk is clearly on a high data density storage medium for everyday usage.

If we would like an archival storage system however, the 10 years storage time of the hard disk is very short. When we want to store information for longer timescales we would likely move to a different storage medium, for instance archival grade DVD's. These DVD's however, will only survive for the predicted 100 years if they are stored in a proper environment. Storing information for an even longer time, while having a reasonable data density, would be possible by storage on acid-free archival paper, which should last for about 500 years. But these 500 years will only be achieved when the paper is stored in a low humidity, constant temperature environment.

So what if we want a medium to store information which will outlast the human race itself (Manz, 2010)? Such a medium could be used to show mankind's greatest achievements, depict works of art, which themselves can not survive this long or even hold the key to rebuilding society. This would require a medium with high energy barriers, most likely at the cost of data density.

The required lifetime of such a medium should be 1 million up to 1 billion years (Elwenspoek, 2011) and likely needs to be specifically designed for this purpose. Here the energy barrier should not be low enough to ensure a high data density which lasts for 10 years, but foremost high enough to last for at least a million years without severe loss of data.

In chapter 5 a medium is designed specifically for the purpose of surviving for a very long time. An accelerated ageing test is performed to determine whether the medium will survive for 1 million years or longer by storing the medium at an elevated temperature.

Chapter 2

Separation of nucleation and depinning field for single islands

2.1 Introduction

To continue the areal bit density growth in magnetic recording beyond the limits set by thermal fluctuations, bit patterned media (BPM) are required in which each bit is a single domain nano-magnetic island (Chou et al., 1994). An important requirement for BPM is a narrow switching field distribution (SFD) of the array of islands. In many instances, the SFD is too large for fault-less writing (Shaw et al., 2007; Thomson et al., 2006). To decrease the width of the SFD, it is crucial to understand the origins of the SFD for patterned elements. These origins can be found in fundamental physical and intrinsic magnetic properties such as anisotropy, magnetisation, and exchange coupling (Shaw et al., 2007; Thomson et al., 2006).

In order to understand the mechanisms determining the switching field, we investigate the switching behaviour of magnetic islands by means of the highly sensitive Anomalous Hall Effect (AHE). This effect, in addition to the normal Hall voltage, is observed in ferromagnetic materials and is proportional to the out-of-plane component of the magnetisation (Sinitsyn, 2008). Contrary to other techniques sensitive enough to sense reversal of individual magnetic islands like μSQUID (Wernsdorfer et al., 1997) and magnetic force microscopy (Belle et al., 2007; Thomson et al., 2006), AHE measurements can be performed in a wide temperature range, including room temperature, and does not require extensive sample preparation.

We have previously used this method to detect the magnetic reversal of individual islands inside an array, by carefully analysing steps in the AHE voltage when the magnetic field is swept. By taking thousands of measurements, the switching field distribution induced by thermal activation of an individual island inside an array of islands was measured, from which we in principle can de-

This chapter is based on (Delalande et al., 2012)

termine the energy barrier and switching volume of each single island (Engelen et al., 2010). However, a large distribution in the size of the voltage steps was observed, which complicates interpretation of the data. Assuming a homogeneous island size in the array, a relatively small step size could either be assigned to the magnetic reversal of a small nucleus inside an island, or the switching of an entire island positioned in a less sensitive part of the cross (Alexandrou et al., 2010).

In order to exclude the latter possibility, we explore in this chapter the reversal mechanism of a single Co/Pt island prepared by e-beam lithography. We use AHE to be able to detect partial reversal of the island and Magnetic Force Microscopy (MFM) to investigate the magnetisation state.

2.2 Experimental

Multilayer stacks of [Co (0.4 nm)/Pt (1 nm)]$_5$ were deposited on thermally oxidised SiO_2 ⟨100⟩ substrates with Pt (30 nm) buffer layers by magnetron sputtering. The Pt layers were deposited at a rate of 6.0 nm min^{-1} and the Co layers at a rate of 0.9 nm min^{-1} under a sputtering pressure of 1 Pa. The Pt seedlayer promotes the ⟨111⟩ crystal growth, required to get perpendicular anisotropy (Canedy et al., 2000). A 3 nm thick Pt layer serves as a capping layer to protect the Co from oxidation.

Cross shapes were defined in the Pt/[Co/Pt] stack using optical lithography and ion beam etching. The Hall cross is patterned directly into the Pt seed layer, which allows for a better electric conductivity between the island and the cross than when the Pt cross shape is deposited on top of the magnetic island. On the resulting Pt/[Co/Pt] crosses, single islands were written in hydrogen silsesquioxane (HSQ) resist using e-beam lithography with diameters of 250 nm and 350 nm. The resist island is transferred into the magnetic [Co/Pt] layer by means of ion beam etching.

The resulting samples contain a single magnetic [Co/Pt] island on top a Pt cross (figure 2.1), suitable for AHE measurements. These are performed at a controlled temperature of 293 K, in a 2300 kA m^{-1} superconducting magnet. The field is applied at varying angle θ, defined as the angle between the direction of the applied magnetic field and the direction perpendicular to the sample plane. A drive current of 1 mA runs through the cross at a frequency of 133 Hz, which allows for the detection of the Hall voltage by means of a lock-in amplifier. A measurement was performed every 3 s while the magnetic field was swept between the sample saturation levels at a rate of 2.5 kA m^{-1} s^{-1}. Although the ordinary Hall effect (OHE) is also influenced by the variation in angle it is mostly prominent at higher fields.

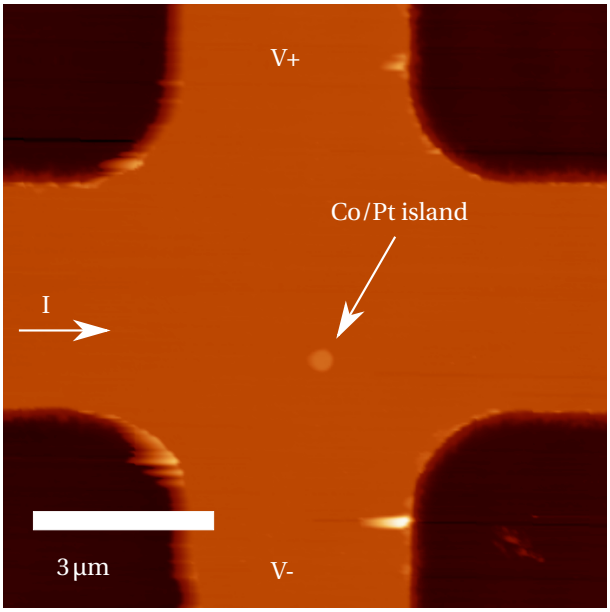

FIGURE 2.1 – *AFM image of a Pt Hall cross with a single 350 nm Co/Pt island*

2.3 Results and Discussion

2.3.1 Structure and magnetic properties of the continuous film

The continuous film was characterised prior to patterning. X-ray diffraction patterns indicate that Co/Pt thin films are (111) textured with rocking curve widths of the CoPt (111) peak of 15°. Grazing incidence X-ray reflectivity analysis shows that the thin films have a roughness of around 0.5 nm, which is relatively high compared to the individual layer thicknesses. However, TEM cross-section clearly shows that the roughness is conformal from one layer to the next and the layering still exists on a finite lateral length scale (figure 2.2).

By means of a home built torque (TMM) and vibrating sample magnetometry (VSM), the effective anisotropy constant K_{eff} and saturation magnetisation M_s were determined to be 240 kJ m^{-3} and 450 kA m^{-1}, respectively. The effective anisotropy results from the competition between the intrinsic perpendicular anisotropy K_u and the shape anisotropy of the thin film ($1/2\ \mu_0 M_s^2$, using the SI unit system). Square hysteresis loops with remanence close to 0.92 are obtained when measured with an applied magnetic field perpendicular to the sample surface, indicating a perpendicular easy axis (figure 2.3).

We measured hysteresis loops by AHE on a Hall cross formed by the magnetic film itself for different values of the applied field angle θ (measured with respect to the sample normal). Assuming an exchange stiffness constant (A) of

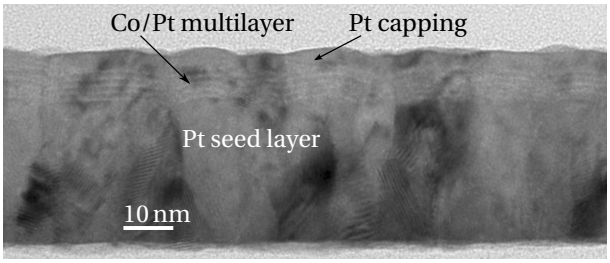

FIGURE 2.2 – *Cross-sectional high resolution TEM image of the [Co(0.4 nm)/Pt (1 nm)]$_5$ continuous film.*

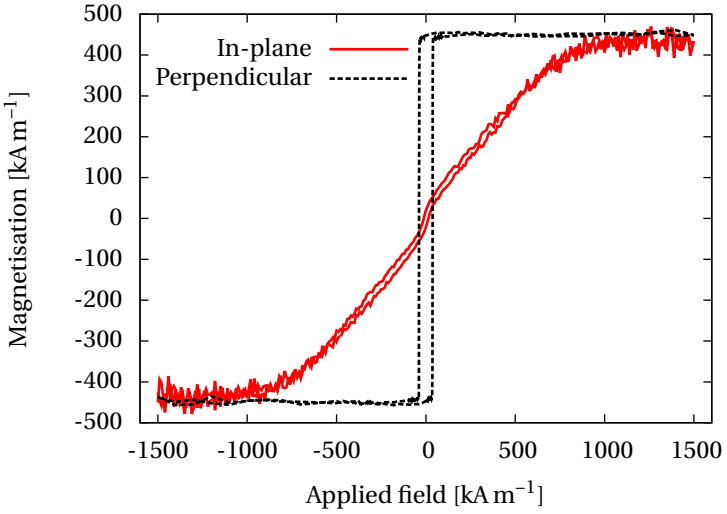

FIGURE 2.3 – *In-plane and perpendicular hysteresis loops measured for the [Co(0.4 nm)/Pt (1 nm)]$_5$ continuous film.*

1.8 pJ m^{-1} (Zeper et al., 1991) the domain wall width $\left(\pi\sqrt{A/K_{\text{eff}}}\right)$ is found to be 8.6 nm and the exchange length $\left(\sqrt{2A/\mu_0 M_s^2}\right)$ is found to be 4 nm. Since the cross dimensions are large compared to the film thickness, domain wall width and exchange length, the Hall cross area can in essence be considered as a thin film. Figure 2.4 shows the reversal field against θ. This curve fits very well to the Kondorsky reversal model for weakly pinned domain walls ($1/\cos(\theta)$ relation), which shows that magnetisation reversal in the continuous film primarily takes place by domain wall movement. The domain wall pinning field in the continuous film was determined from the fit to be $H_{\text{p,film}}$=43 kA m^{-1}.

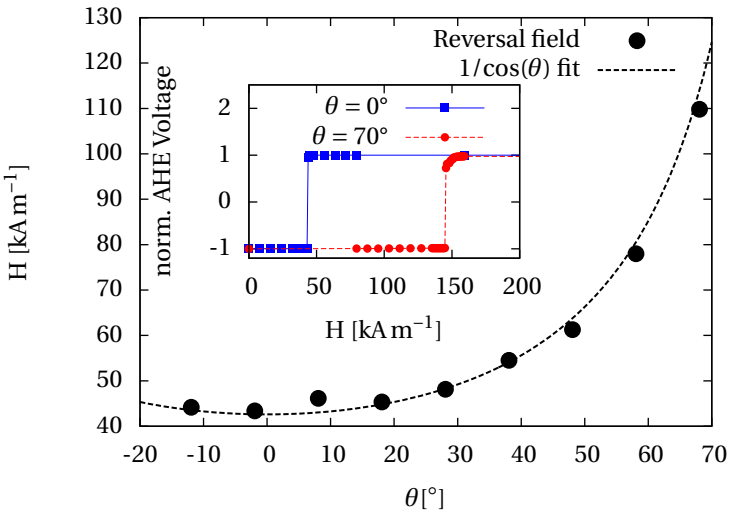

FIGURE 2.4 – *Angle dependent measurements of the reversal field measured by AHE. The dotted line is the best fit with Kondorsky function (1/cos(θ)).*

2.3.2 Angular dependence of the nucleation field of a single island

AHE hysteresis loops of the single Co/Pt islands with a diameter of 250 nm and 350 nm were measured for angles θ varying from 0° to 85°. For field angles up to 80° only a single step, corresponding to the complete magnetic reversal of the island (Alexandrou et al., 2010; Engelen et al., 2010), was measured for each island. When plotted against the angle θ the reversal field of the single Co/Pt island exhibits a Stoner-Wohlfarth (SW)-like angular dependence with a minimum close to 45° (figure 2.5). However, deviations from the coherent rotation model are observed since the curve shows an asymmetry, and the minimum switching field is not half of the value at 0°, as predicted by the SW model. This angular dependence can be reproduced however by the modified Kondorsky model, which combines domain wall motion and rotation of the magnetisation in the domains, described by Schumacher (1991) and explained in appendix A. As seen in figure 2.5, the modified Kondorsky model fits very well to our data with an effective anisotropy field H_{Keff}=396(11) kA m^{-1} and a pinning field at zero angle (normalised to H_{Keff} as $h_{\mathrm{p}}(0°)=H_{\mathrm{p}}(0°)/H_{\mathrm{Keff}}$) $h_{\mathrm{p}}(0°)$=0.63(3) for the 350 nm island. The fitting parameters are H_{Keff}=531(30) kA m^{-1} and $h_{\mathrm{p}}(0°)$=0.47(5) for the 250 nm island.

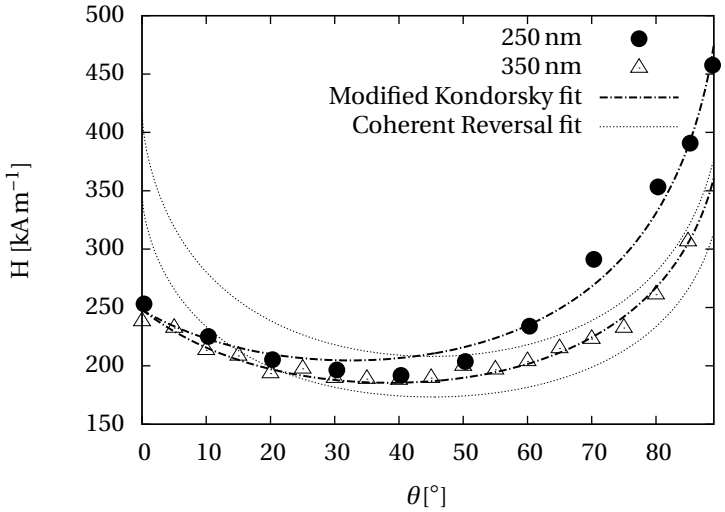

FIGURE 2.5 – *Angular dependence of reversal field of single Co/Pt islands with two different diameters. The dash-dotted lines show the best fit to the modified Kondorsky model and the dotted lines the best fit to the coherent reversal model.*

2.3.3 Angular dependence of the depinning field of a single island

For the 350 nm island, increasing the angle θ beyond 80° leads to two steps in the Hall voltage, indicating that the single island switches in two parts. MFM images taken after the first step in the AHE voltage (in the remanent state) reveal that after the first step the island has two magnetic domains, separated by a domain wall (figure 2.6).

In order to study the depinning field of this domain wall, the magnetic state of the island was initialised in the two-domain state by applying a magnetic field with an angle of 85° until the first step was observed in the AHE voltage. After removing the magnetic field, the angle θ is adjusted in the range from 0° to 85° and the magnetic field is increased again until a step in the AHE voltage is observed, indicating that the magnetic state of the island has now completely reversed. This step corresponds to the depinning and subsequent propagation of the domain wall throughout the whole island. By repeating this procedure for different field angles, while recording the magnetic field value necessary to depin the domain wall for different angles, one can determine the angular dependence of the depinning field (figure 2.7). The angular dependence of the domain wall propagation fits well with a $1/\cos(\theta)$ curve (Kondorsky model), as expected for domain wall motion reversal with weak pinning. The fit results in a pinning field value of $H_p(0°)$=35 kA m^{-1}.

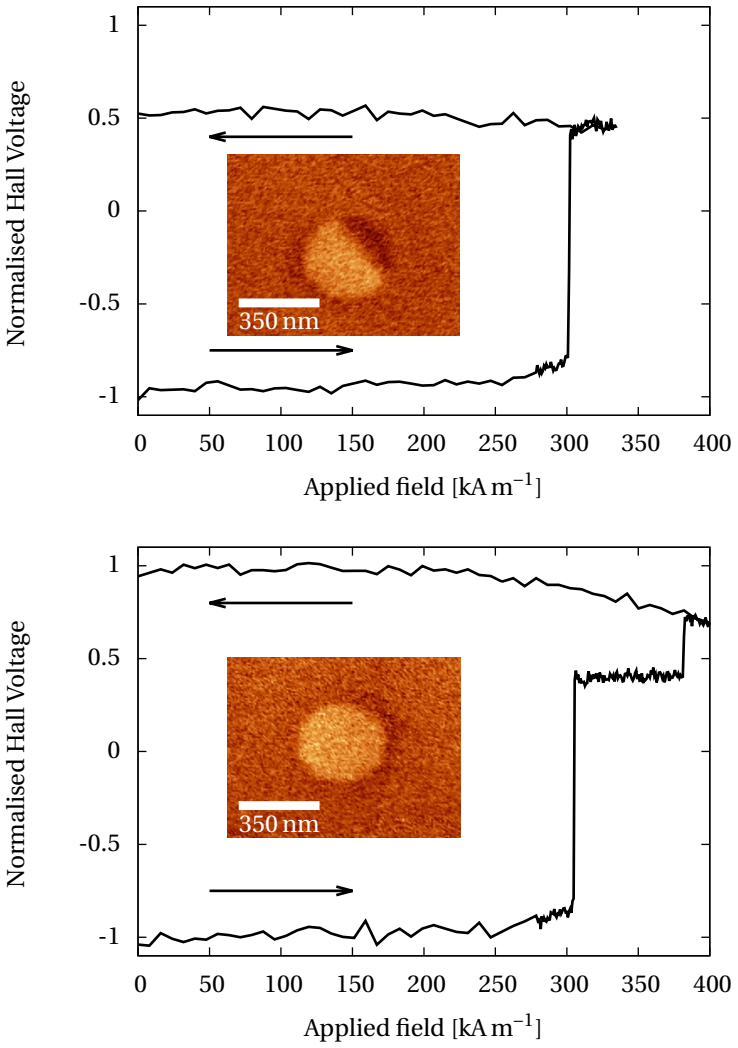

FIGURE 2.6 – *Hall measurement (θ=85°) indicating switching in two steps and the corresponding MFM (remanent state) images revealing two domain states.*

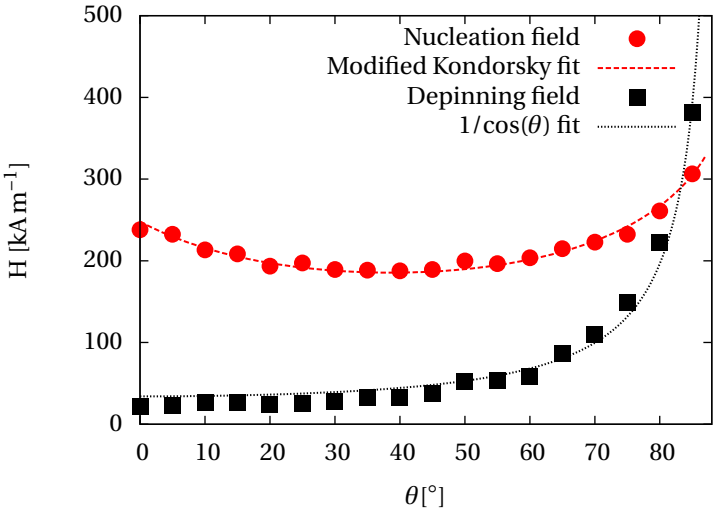

FIGURE 2.7 – *Angle dependent measurements of the required field for nucleation and depinning. Dotted lines indicate the best fit with the modified Kondorsky function for the nucleation field and* $1/\cos(\theta)$ *function for depinning field. At angles larger than 85°, the two domain state can be induced in the island.*

2.4 Discussion

Our observations confirm the model by Thomson et al. (2006), which suggests that reversal of large islands takes place by nucleation of a reversed domain at a nucleation field H_n and subsequent propagation of a domain wall through the island. At field angles close to the film normal, the field required for nucleation of a reversed domain (about 250 kA m^{-1}) exceeds the field for depinning of the domain wall (35 kA m^{-1}) and the two-domain state is never observed. In our case however, we succeeded in trapping the domain wall at near in-plane field angles. Due to the $1/\cos(\theta)$ variation of the depinning field, there is an angle θ (figure 2.7) for which the depinning field H_p exceeds the nucleation field H_n and the wall is pinned at a defect. The presence of a stable, strongly pinned domain wall suggests an inhomogeneity in magnetic properties (intrinsic anisotropy, exchange constant and saturation magnetisation) inside the island. The similarity between the pinning field of the domain wall in a continuous film and in the island suggests that the defect resulting in the domain wall pinning was already present before patterning (The pinning of the domain wall by the cross corners is estimated at 1.6 kA m^{-1} (Cayssol et al., 2002) and therefore can be neglected). This observation is in agreement with measurements by Lau et al. (2008) and Hauet et al. (2011), who attribute the defect to misaligned grains.

Even though the modified Kondorsky model reproduces the experimental

angular dependence of the nucleation field well, one should be careful when attributing physical significance to fitting parameters, such as the depinning field H_p. The modified Kondorsky model assumes the existence of a strongly pinned domain wall before switching, which might not be the case in our situation. Incoherent rotation seems to be a more relevant reversal mechanism. Moreover, the modified Kondorsky model suggested by Schumacher is set up for a continuous film, whereas in our case we have a patterned element. Magnetic calculations made by Uesaka et al. (1995) on magnetic hexagonal particles with perpendicular magnetic anisotropy show that a region of low anisotropy at a corner of the particle results in an asymmetric angular dependence of the switching field as well. In our case etching damage or redeposition of a magnetic layer on the edge of the island during etching could be the origin of anisotropy reduction (Shaw et al., 2008). It should be noted however that the demagnetisation field is smaller at the edge of a perfect island, so in principle nucleation of a reversed domain should start in the centre of the island. The reduction of anisotropy at the edge of the island should be quite severe (Shaw et al., 2008).

2.5 Conclusion

From AHE and MFM measurements we conclude that magnetic reversal of Co/Pt multilayered islands with diameters of 250 nm and 350 nm and a perpendicular anisotropy takes place by nucleation of a reversed domain followed by propagation of the domain wall through the island. The domain wall can be trapped in the island at near in-plane field angles (85° with the magnetic easy axis). By measuring the angular dependence of the field required for depinning the domain wall, we conclude that the depinning field is accurately predicted by the Kondorsky model ($1/\cos(\theta)$). The angular dependence of the nucleation field resembles a more Stoner-Wohlfarth-like behaviour however, which can be accurately fitted to modified Kondorksy model for strongly pinned domain walls.

Chapter 3

Statistical measurements on patterned media

3.1 Introduction

Bit patterned media are firmly on the roadmap as a medium for future hard disk technologies. Most likely in combination with heat assisted recording, bit patterned media are considered as the last and final stage in pushing the superparamagnetic effect to its fundamental limit (Terris et al., 2007).

One of the most prominent obstacles that needs to be overcome before commercialisation is possible, is the large variation in required switching field between the islands that define the single bits. The origin of this switching field distribution (SFD) is most likely already present in the magnetic film before patterning (Shaw et al., 2007; Thomson et al., 2006). Variations in magnetic anisotropy in the film lead to a variation in energy barrier against reversal for individual islands and therefore a variation in switching field. Since magnetic reversal is thermally activated at room temperature, the relation between energy barrier and switching field is complex and cannot be easily separated. A common solution to this problem is to measure the switching field as a function of temperature, and extrapolate to 0K. As material properties are a function of temperature as well, this method does not lead to an accurate determination of the energy barrier at room temperature. Another solution is to measure the switching field as a function of field sweep rate. Due to restraints on the signal-to-noise ratio (SNR), it is very challenging to perform this method on single islands.

To determine the energy barrier of a single island at room temperature, we have taken an alternative approach (Engelen et al., 2010). The thermal energy leads to fluctuations of the switching field of an individual island. When taking many hysteresis loops, these fluctuations result in a thermal switching field distribution (SFD_T). Using the high sensitivity of the anomalous Hall effect

This chapter is based on de Vries et al. (2013)

(AHE), it has become possible to take hundreds of hysteresis loops of a single island in a relatively short period. From statistical analysis of the switching fields for a single island, we can extract the energy barrier in the absence of an external magnetic field (E_0) and the switching field in the absence of thermal fluctuations (H_s^0).

Due to the large SFD it is possible to isolate a weak and a strong island which are present at the extremities of the distribution and determine their energy barriers. This makes it possible to compare the energy barrier of an island which requires a low switching field to the energy barrier of an island requiring a high switching field.

3.2 Experimental

3.2.1 Thin film fabrication

Multilayers

The magnetic multilayer samples were prepared by cleaning ⟨100⟩ wafers and stripping the native oxide.* A thermal oxide layer of 50 nm is grown in an LPCVD furnace which acts as an insulating layer between the conducting metal layer and the bulk silicon. A VSW DC sputtering system is used to deposit all metal layers in one single run. The thickness of each layer is controlled by opening and closing of the shutters in front of the sputter guns. The base pressure of the system was lower than 0.5 µPa. The Ar sputtering pressure was 1 Pa for the Ta layers and 0.8 Pa for the Co and Pt.

The seedlayers for both multilayer samples consist of 5 nm Ta and 25 nm Pt. A bilayer of 0.3 nm Co and 0.3 nm Pt is deposited with 5 repetitions resulting in a 3 nm magnetic layer and 34 repetitions resulting in a 20 nm magnetic layer. The capping for both samples consists of 3 nm Pt, which prevents oxidation of the Co. The 3 nm multilayer will sometimes be referred to as Ml 3 nm and the 20 nm multilayer as Ml 20 nm.

Alloy

A $Co_{80}Pt_{20}$ alloy sample was fabricated by DC magnetron sputtering using a home built sputtering system with a base pressure of 3 µPa and a sputtering pressure of 0.5 Pa. On a thermally oxidised substrate a layer of 5 nm Ta, 5 nm Pt and 20 nm Ru were deposited followed by a layer of 20 nm $Co_{80}Pt_{20}$, with a capping of 2 nm Pt. All layers were deposited in a single run. This sample will be referred to as alloy I.

Previously a $Co_{80}Pt_{20}$ alloy was investigated which consisted of 5 nm Ta, 10 nm Pt and 20 nm Ru with 20 nm $Co_{80}Pt_{20}$ and a 2 nm Pt capping (Engelen et al., 2010). The metal layers were deposited by magnetron co-sputtering at

*For a detailed process flow of the patterned media, please refer to appendix B

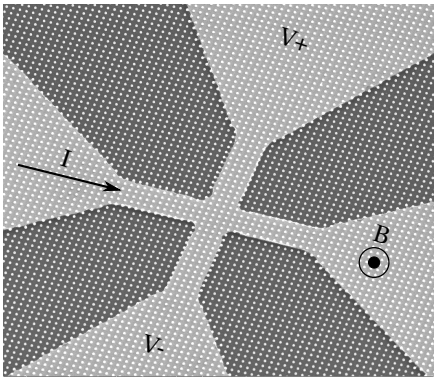

FIGURE 3.1 – *SEM picture of a Hall cross structure with the islands with a 220 nm diameter and 600 nm pitch on top. The direction of the current (I), magnetic field (B) and measured Hall voltage (V) are indicated by their symbols.*

room temperature. This alloy will be referred to as alloy II and results from both multilayers and alloy I will be compared to previous results from this alloy.

3.2.2 Patterning of arrays of islands

Both multilayers and alloy I are patterned using the same steps. Laser interference lithography (LIL) is used to create a mask of photoresist by two maskless exposure steps under an angle of 90°.

The pattern is first transferred into the bottom anti-reflective coating (BARC) by O_2 reactive ion beam etching (RIBE). This layer of BARC limits standing waves caused by interference of the incoming waves with reflections from the metal layers. The BARC layer that we use is DUV-30 J8. The pattern is then transferred into the magnetic layer by Ar ion beam etching (IBE). All etching steps were done in an Oxford i300 reactive ion beam etcher.

After etching, the multilayer samples consist of a Ta/Pt seedlayer with magnetic islands on top and the alloy consists of a Ta/Pt/Ru seedlayer with magnetic islands on top. The average diameter of the islands is approximately 220 nm with a center-to-center pitch of 600 nm.

A standard optical lithography process is used to define Hall cross structures in photoresist. The Hall cross structures are transferred into the insulating layer using Ar IBE to ensure that during the Hall measurement, the current only runs through a small ensemble of islands.

The resulting structure consists of a conducting Hall cross of Pt with magnetic islands with a diameter of 220 nm and a pitch of 600 nm on top as shown in the SEM micrograph in figure 3.1.

Alloy II was also patterned using LIL but the etching steps consisted of O_2 plasma etching to transfer the pattern into the BARC layer and Ar IBE to transfer

the pattern into the magnetic layer. The IBE step was performed on a different (home built) system.

3.2.3 Magnetic Analysis

To determine the effective anisotropy a home built torque magnetometer is used capable of applying fields up to 1400 kA m^{-1} under varying angles.

A VSM-10 vibrating sample magnetometer is used to measure the continuous film before patterning to determine the saturation magnetisation. The patterned 20 nm multilayer sample is also measured to determine the switching field distribution before the etching of the Hall cross.

The anomalous Hall effect (AHE) is used to measure the reversal behaviour of the patterned media. Due to the high SNR it is possible to measure the switching field distribution as wel as the reversal behaviour of the individual islands. The measurements are performed on both multilayer samples and alloy I, which are patterned and contain Hall cross structures. For the AHE measurements a home built setup is used where a magnetic field can be applied of up to 1000 kA m^{-1} perpendicular to the sample plane. An AC current is provided at 12 333 Hz and the Hall signal is measured using a lock-in amplifier.

A MOKE measurement can be used to measure the SFD of a small ensemble of islands without the need of a Hall cross structure. This makes it possible to compare the SFD of the patterned media before and after etching of the Hall cross to determine whether SFD broadening occurs due to Hall cross etching. The MOKerr measurements have been done using a home built MOKerr setup which is capable of applying fields up to 800 kA m^{-1}. The setup has a 532 nm laser with a spotsize between 1 and 1.5 µm (Alexandrou, 2010).

3.2.4 Structural Analysis

TEM and STEM

To use transmission electron microscopy (TEM) it is necessary to have a sample which is transparent to an electron beam. The preparation of these samples is done by grinding and subsequent ion beam milling. For highly detailed imaging the sample thickness should be lower than 50 nm but the ion milling causes damage to the layers of a few tenths of nanometers. Therefore images were taken in a slightly thicker part than what would have been optimal for highest resolution imaging.

For both multilayers, the continuous as well as the patterned films were prepared for TEM analysis. For alloy I only the continuous film was prepared.

First a bright field Philips CM300ST transmission electron microscope was used to determine the diameter of the grains and inspect the stacking of the multilayer. The patterned sample was specially used to inspect the edge of an island.

Due to the limited resolution of regular TEM, a dark field scanning transmission electron microscope (STEM) FEI TITAN was used on the same samples. This STEM makes it possible to expose the multilayer by material contrast and make it possible to see how the multilayer continues from one grain to the next.

3.3 Theory

3.3.1 Thermal switching field distribution

Using a theory based on the Arrhenius law and field rate dependent switching we are able to estimate the energy barrier in the absence of an external field (E_0) and the switching field in the absence of thermal fluctuations (H_s^0).

The chance that an island has not reversed magnetisation yet after time t under application of a magnetic field H is (Neél, 1949; Wernsdorfer et al., 1997):

$$P_{\overline{\text{sw}}}(\Delta t) = \exp\left(-\Delta t/\tau(H,T)\right),$$
$$\tau(H,T) = f_0^{-1}\exp\left(\frac{E_\text{b}(H)}{\text{k}_\text{B}T}\right)$$

The probability density is then given by (Wang et al., 2004):

$$p_\text{sw}(H,T) = \frac{f_0}{R}\exp\left(\frac{-E_\text{b}(H)}{\text{k}_\text{B}T}\right) \times \exp\left[-\frac{f_0}{R}\int_0^H \exp\left(\frac{-E_\text{b}(h)}{\text{k}_\text{B}T}\right)\text{d}h\right] \tag{3.1}$$

Where f_0 is the attempt frequency, assumed to be 1 GHz (Weller and Moser, 1999), $E_\text{b}(H)$ is the field dependent energy barrier, k_B is the Boltzmann constant and T the temperature in Kelvin. The field sweep rate is given by R.

3.3.2 Reversal

Reversal by domain wall movement

The energy barrier $E_\text{b}(H)$ in equation (3.1) depends on the reversal mechanism and is field dependent. In the case of incoherent rotation caused by domain wall movement, the field dependent energy barrier ($E_\text{b}(H)$) is given by Gaunt (1986) and described in appendix C:

$$E_\text{b}(H) = E_0\left(1-\frac{H}{H_s^0}\right) \tag{3.2}$$

For the domain wall movement model, the relation between the nucleation volume (V) and energy barrier in the absence of an external field (E_0) is given by Gaunt (1986) (appendix C):

$$E_0 = 2\mu_0 M_s H_s^0 V \tag{3.3}$$

With μ_0 being the vacuum permeability and M_s is the saturation magnetisation.

Coherent reversal

The second model for $E_b(H)$ is a model for Stoner-Wohlfarth reversal or coherent reversal. Here the field dependent energy barrier ($E_b(H)$) is given by Victora (1989) and shown in appendix D:

$$E_b(H) = E_0\left(1 - \frac{H}{H_s^0}\right)^2 \tag{3.4}$$

This $E_b(H)$ differs from the incoherent rotation model only by its exponent n, therefore the domain wall movement model will be referred to as the "n=1 model" and the coherent rotation model as the "n=2 model".

Here the relation between energy barrier and volume is given by Sharrock and McKinney (1981) (appendix D):

$$E_0 = \frac{1}{2}\mu_0 M_s H_s^0 V \tag{3.5}$$

Elevated temperature

Both models relating the volume and the energy barrier are valid at 0 K. Because our measurements are performed at room temperature, the measured switching field H_s^0 is not equal to the switching field at 0 K. To determine the switching field value at room temperature we determine the maximum of the probability density of the switching field (equation (3.1)) by solving the value of H_s^0 for which $\frac{\partial p_{sw}}{\partial H} = 0$. This gives us the average of the thermal switching field distribution, which is the average switching field at room temperature.

3.4 Results

3.4.1 Magnetic properties of continuous films

Multilayers

The saturation magnetisation of the continuous thin film (M_s) was determined to be 870(40) kA m^{-1} and 829(60) kA m^{-1} for the 3 nm and 20 nm multilayer respectively from VSM measurements.

The effective anisotropy K_{eff} was measured using a torque meter and found to be 405(1) kJ m^{-3} for the 3 nm and 386(1) kJ m^{-3} for the 20 nm multilayer. This results in an uniaxial anisotropy of $\left(K_u = K_{eff} + \frac{1}{2}\mu_0 M_s^2\right)$ of 902 kJ m^{-3} for the 3 nm multilayer and 818 kJ m^{-3} for the 20 nm multilayer. Using the relation $H_{Keff} = 2K_{eff}/\mu_0 M_s$ (Lambert et al., 2013) we find a H_{Keff} of 743(36) kA m^{-1} and 734(55) kA m^{-1} for the 3 nm and 20 nm film respectively.

Alloy

The saturation magnetisation for alloy I was determined to be 1070(60) kA m^{-1} by VSM and the K_{eff} 435(1) kJ m^{-3} by torque meter. The uniaxial anisotropy, K_{u}, is 1160 kJ m^{-3}. The H_{Keff} was found to be 732(45) kA m^{-1}.

Alloy II had an M_{s} of 1200 kA m^{-1} and a of K_{u} of 1300 kJ m^{-3}. The effective anisotropy, K_{eff}, is 395 kJ m^{-3}. The errors on M_{s} and K_{eff} are expected to be similar to the errors on the alloy and multilayer measurements. The H_{Keff} was previously found to be 540 kA m^{-1}.

Comparison

It is clear the M_{s} and K_{u} are comparable for the multilayer samples but are much higher for the both alloy samples, with alloy II having the highest values.

The effective anisotropy K_{eff} however is comparable for all magnetic layers before patterning.

The H_{Keff} is comparable for both multilayer structures and alloy I but is higher than the value found for alloy II.

3.4.2 Structure

Multilayer

Figure 3.2 a and b show bright field TEM cross-sectional images of the 3 nm and 20 nm multilayer films. We can clearly see a columnar growth extending into the multilayer, which is visible as a bright band towards the top of the film. The growth of the columns seems to be competing as can be seen from the taper of the grains and the difference in contrast of the grains indicates a variation in crystal orientation. The width of the grains varies from approximately 10 nm to 20 nm, although some grains have a taper which makes it difficult to give a single value for their grain size.

From the dark field STEM images we can see the 3 nm multilayer in figure 3.3 a and b. Because this is a dark field image, the material contrast is inverted and the Pt is bright compared to the Co, as opposed to the TEM images from figure 3.2. From figure 3.3 a we can clearly see the dark band which contains the Co. The separation of the layers can be seen within this dark band. The edge of a single island of the patterned 3 nm multilayer can be seen in figure 3.3 b. The multilayer is visible up to approximately 3 nm from the edge. If mixing of the multilayer has occurred due to the etching process, which we can not be certain of, it is likely less than 3 nm.

The STEM image of the 20 nm multilayer can be seen in figure 3.3 c. In this image the modulation of the Co/Pt layer can also clearly be seen. The stacking of the multilayer is visible all the way to the top, but the stacking is not perfect due to the roughness of the substrate, variation in crystal orientation and mismatch of the Co and Pt lattice.

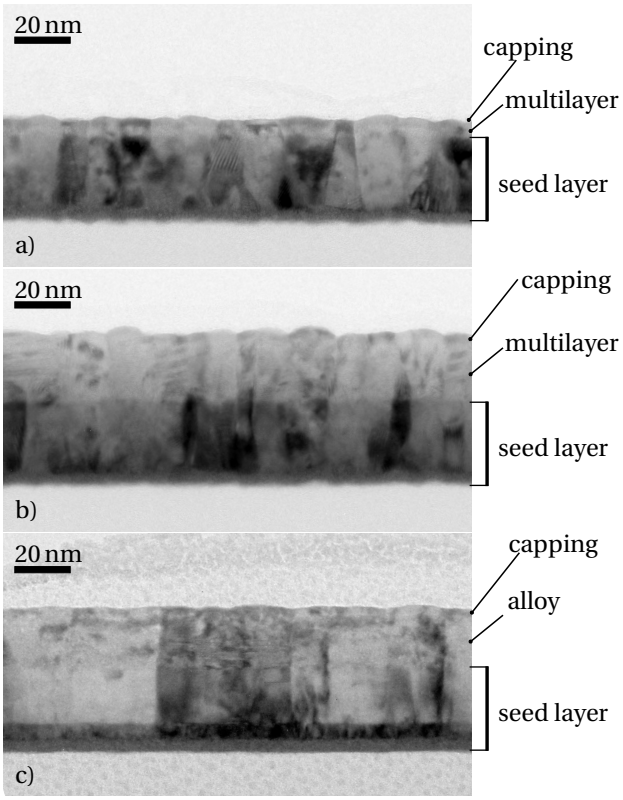

FIGURE 3.2 – *TEM pictures of the a) 3 nm multilayer b) 20 nm multilayer c) 20 nm alloy.*

The FWHM of the (111) CoPt peak was ≈12° for both multilayers and was found by rocking curve measurements using a Philips X'Pert 1 diffractometer on the continuous films.

Alloy

Figure 3.2 c) shows a bright field TEM cross-sectional image of the alloyed film. For alloy I the grains seem to be around 15 nm. Also there seems to be less competition between the grains in the alloy, as can be seen by the better defined columnar growth. For alloy II the average grain size was previously estimated to be 14 nm (Engelen et al., 2010).

The dark field STEM image of alloy I in figure 3.3 d clearly shows a crystalline growth which extends from the Ru into the $Co_{80}Pt_{20}$ layer. From the STEM images it is clear that the crystal orientation and stacking of alloy I is much better defined than the crystal orientation and stacking of the multilayers. This

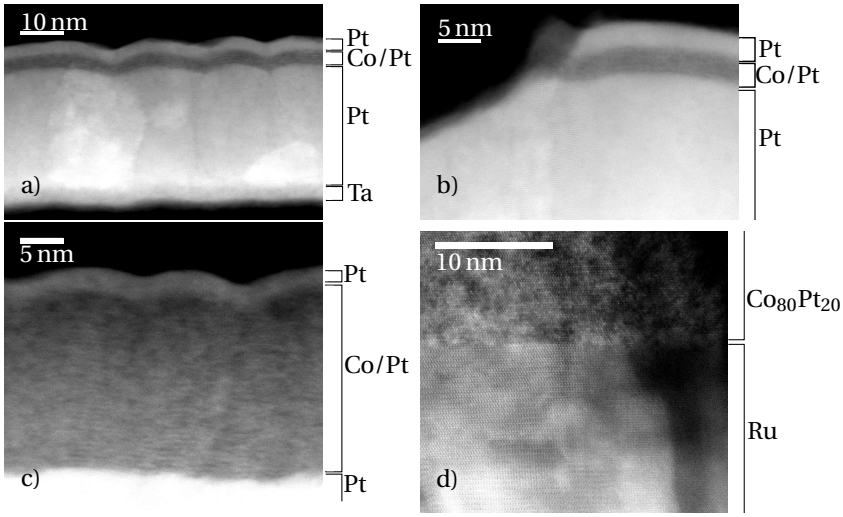

FIGURE 3.3 – *Dark field STEM images of a) the cross section of the 3 nm multilayer b) the edge of the patterned 3 nm multilayer c) 20 nm multilayer d) $Co_{80}Pt_{20}$ film.*

is likely caused by a much better seedlayer.

The FWHM of the rocking curves measurements of alloy I gave a c-axis distribution of ≈ 3.5°. The c-axis distribution for alloy II was ≈ 2.8° (Engelen et al., 2010).

Comparison

From the TEM images we found that the width of the grains of both the multilayer samples and alloy I are comparable to the width of the grains in alloy II.

The distribution of the c-axis however is much smaller for the alloys than for the multilayer samples, indicating that the orientation of the grains is much better in both of the alloy samples.

3.4.3 Magnetic properties of arrays of islands

Figure 3.4 shows the hysteresis loops of arrays of islands fabricated from the two multilayers and alloy I, measured by Hall magnetometry. We find that the switching field distribution (SFD) is smaller for the two multilayer samples than for the alloy sample. The switching fields for the 3 nm multilayer are higher than for the 20 nm multilayer. This might be caused by the slightly higher anisotropy for the 3 nm film or larger etching damage to the 20 nm film.

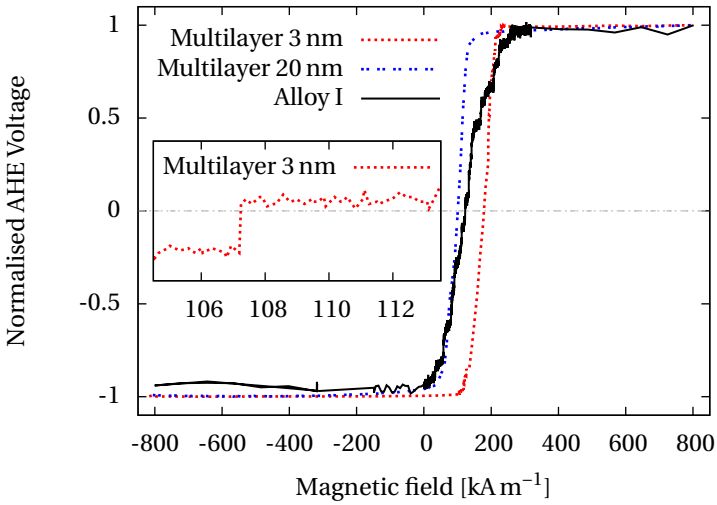

FIGURE 3.4 – *Hall curves of the 3 nm and 20 nm multilayer and the 20 nm alloy. The voltage step in the inset shows reversal of a single island in the 3 nm multilayer.*

Figure 3.5 shows half of the hysteresis loop measured by VSM, AHE and MOKE. The sample used in the VSM and MOKE measurement is the patterned 20 nm multilayer without a Hall cross, whereas the AHE measurement is done on the 20 nm multilayer with a Hall cross. The VSM measures the entire sample which not only contains the islands but also a small part of continuous film which was shielded during etching. Both the AHE and the MOKE only measure a small part of the sample.

Due to the large SFD it is likely that the AHE which measures only ~80 islands and MOKE which measures ~16 islands, do not capture the entire SFD. This explains why the largest SFD can be seen for the VSM measurement. The larger SFD for the AHE measurement than the MOKE measurement can be explained by the larger ensemble of islands. Furthermore, the VSM also measures all of the resputtered material.

In the VSM measurement, from –100 kA m^{-1} to 100 kA m^{-1}, a linear slope can be seen which can be attributed to the part of continuous film which was shielded during etching. From these measurements there is no indication that the etching of the Hall cross has a large influence on the SFD of the patterned sample.

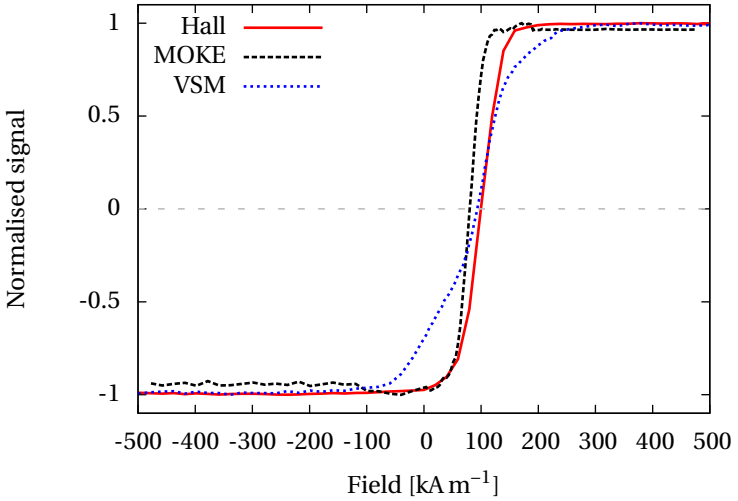

FIGURE 3.5 – *Results of VSM and MOKE measurements on the 20 nm patterned multilayer without a Hall cross and AHE measurements on the 20 nm patterned multilayer with a Hall cross. The patterned sample without a Hall cross contains a small part of continuous film which can be seen in the VSM measurement from –100 kA m^{-1} to 100 kA m^{-1}.*

3.4.4 Statistical analysis of SFD_T

Using the AHE the switching fields of a single weak and strong island are measured over 1000 times to provide sufficient statistics. An example of the distribution of the required reversal field is given in figure 3.6, for the weak island in the patterned 3 nm film. From the fits of equation (3.1) with equation (3.2) for n=1 and equation (3.4) for n=2. The results of the fits to all the measurements of the different samples are given in table 3.2.

From the goodness of fit, it is not clear whether the n=1 or the n=2 model is more suitable. It is likely that both models do not describe the actual reversal because the n=2 model assumes that the whole island reverses coherently, as in a Stoner-Wohlfarth particle. The n=1 model assumes that reversal occurs by domain wall movement when a domain wall is already present in the island. It is likely that the actual reversal model is more complex and reversal of the island starts by incoherent reversal of part of the island after which the formed domain wall propagates through the island, similar to what can be seen in chapter 2. We assume that the n=1 and n=2 models show the most extreme cases of reversal.

It is expected that both reversal models are too extreme and the real values of E_0 and H_s^0 are somewhere between the values for coherent reversal and domain wall movement. As a visual aid the values of both E_0 and H_s^0 are shown in the

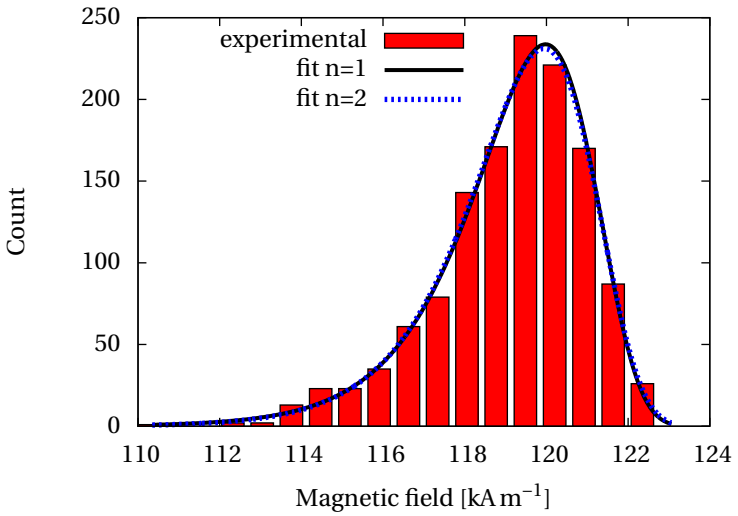

FIGURE 3.6 – *Histograms of the reversal field of the weakest 3 nm island with theoretical fits for n=1 and n=2.*

bar graphs in figure 3.7.

3.5 Discussion

We noticed that both the M_s and K_u of alloy I investigated in this work are comparable to the ones found for alloy II (Engelen et al., 2010). There is however a large variation in switching fields when comparing either the weak islands or the strong islands of both films. This could be an indication that our etching process has caused more damage to the magnetic layer than the etching process previously used by Engelen et al. (2010). This can cause a lowering of the anisotropy.

The energy barrier in the absence of an external field as well as the theoretical switching field in the absence of thermal fluctuations are always larger for islands with a high switching field at room temperature. This goes for arrays of islands based on alloy I as well as for both multilayer films. This result contradicts the previous work on alloy II (Engelen et al., 2010), where it was found that the energy barrier is independent of the switching field. This contradiction could be caused by differences in the etching procedure.

When comparing an alloyed film and multilayer of the same thickness of 20 nm, we observe that the energy barriers are similar for weak as well as strong islands. The weakest islands in these samples also have comparable switching fields. However, the switching field in the absence of thermal fluctuations, as well as the switching field at room temperature, are about a factor of two higher

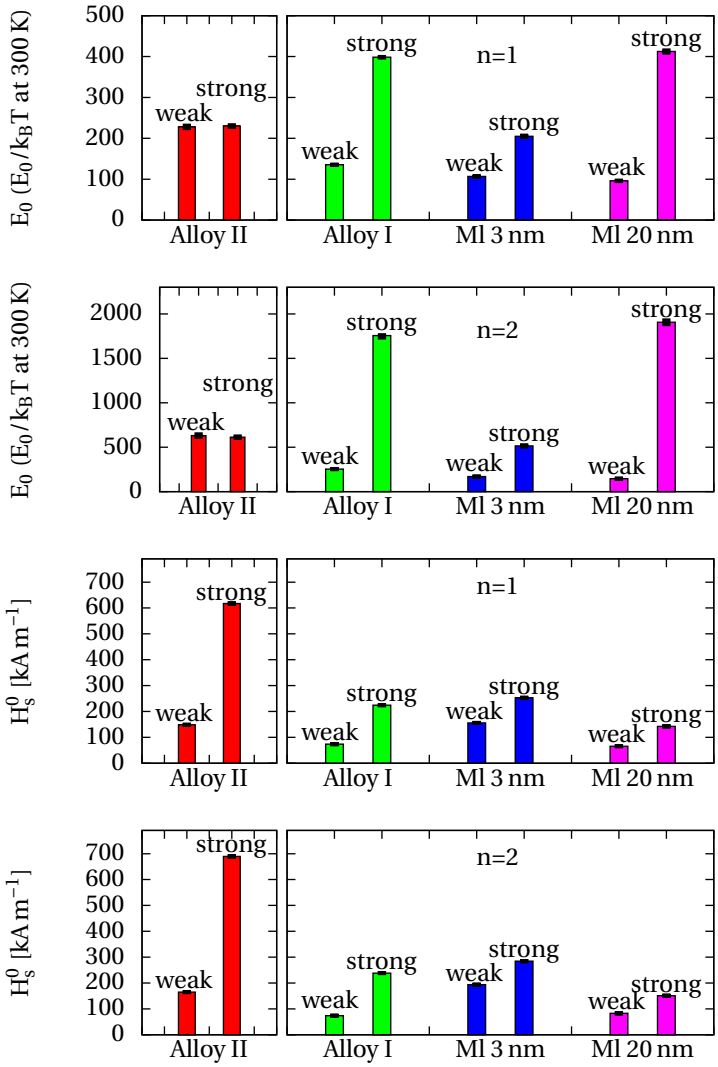

FIGURE 3.7 – *Energy barrier and theoretical switching field in the absence of thermal fluctuations. These parameters are obtained by fitting approximately 1000 reversal incidents measured at room temperature of a weak and strong island in patterned alloyed and multilayered films. Top: Energy barrier n=1, second from the top: Energy barrier n=2, second from the Bottom: H_s^0 n=1, bottom: H_s^0 n=2.*

TABLE 3.1 – *The radius of a cylindrical nucleation volume determined by fitting equation (3.1) to the values for E_0 and H_s^0 found from the distributions (table 3.2) using equation (3.3) and equation (3.5) for the domain wall movement (n=1) and coherent rotation (n=2). The SF is compensated for the measurement at room temperature.*

		radius (nm)	
		n=1	n=2
Sample			
Multilayer 3 nm	weak	8	29
	strong	10	96
Multilayer 20 nm	weak	5	11
	strong	8	36
Alloy I	weak	5	14
	strong	5	25
Alloy II	weak	4	14
	strong	2	7

for the strongest alloyed islands compared to the strongest multilayer islands. This is in agreement with the fact that the uniaxial anisotropy of the continuous alloyed film is considerably higher than that of the multilayered film.

When comparing arrays of islands prepared from 3 nm and 20 nm films, we find that the weakest islands in both films have similar energy barriers. The strongest islands in the 20 nm film however, have an energy barrier which is at least a factor of two higher than the strongest islands in the 3 nm film. The uniaxial anisotropy is higher for the 3 nm film and the switching fields of islands based on this film are a factor of two higher than those prepared from the 20 nm film, for weak as well as strong islands. Apparently, a reduction of switching volume when reducing the film thickness is partly compensated by an increase in anisotropy, which does not correspond to the nucleation volumes found in table 3.1 which shows a similar or larger nucleation volume. This can be attributed to deviations between the model and the actual reversal mechanism, causing deviations from the actual switching volume.

When we look at table 3.1 we see that the nucleation volume increases with an increasing switching field for all samples, except for alloy II. This reduction in volume combined with the increase in anisotropy could cause the energy barrier to remain constant for weak and strong islands. The fact that the nucleation volume increases with the switching field for all other films corresponds to a higher energy barrier for the stronger islands as can be seen in (3.3) and (3.5). We speculate that this might be cause by a minimum nucleation volume, likely related to the grain structure of the film.

TABLE 3.2 – *Energy barriers and switching fields in the absence of thermal fluctuations determined by statistical measurements of the reversal of the weakest and strongest islands of both the 3 nm and 20 nm multilayer and $Co_{80}Pt_{20}$ alloys I and II. The values in parentheses show the 95% confidence intervals obtained from the fitting algorithm. The magnetic field values are given in kA m^{-1}.*

		3 nm		20 nm	
	n	weak	strong	weak	strong
Multilayer					
H_s^{300}		120.0(1)	222.8(1)	49.5(1)	134.4(1)
H_s^0	1	155.7(1)	252.5(3)	65.6(2)	142.6(1)
	2	193.7(1)	284.4(6)	82.9(3)	151.2(1)
E_0/k_BT	1	106.6(1)	205(2)	95.9(6)	412(3)
	2	168.9(4)	515(7)	145(2)	1906(22)
Alloy I					
H_s^{300}				60.5(7)	210.3(8)
H_s^0	1			73.9(0)	224.1(1)
	2			87.9(1)	238.5(0)
E_0/k_BT	1			135(0)	398(1)
	2			253(1)	1754(2)
Alloy II (Engelen et al., 2010)					
H_s^{300}				130.4(0)	539.1(1)
H_s^0	1			148.5(3)	617.2(6)
	2			165.1(5)	690(1)
E_0/k_BT	1			228(3)	230(2)
	2			631(14)	612(9)

3.6 Conclusions

The energy barrier as well as the theoretical switching field in the absence of thermal fluctuations are always larger for islands with higher switching fields at room temperature. This is true for both patterned alloy I as well as the patterned multilayered films.

This result is in contradiction with previous work (Engelen et al., 2010), where it was found that for alloyed films prepared in a similar way, the energy barrier is independent of the switching field. The patterned films in that study however had a two to three times higher anisotropy, most likely due to a more successful etch step leading to less etch damage.

The switching field distribution of arrays based on multilayered films is lower than that of arrays based on alloyed films.

The difference in energy barriers between weak and strong islands is larger for the 20 nm multilayer than for the 3 nm multilayer. This effect is less promi-

nent for the switching field in absence of thermal fluctuations. The variation in energy barrier for the 20 nm multilayer however, is larger than the variation for alloy I.

By determining the radius of a cylindrical nucleation volume we always find that the predicted radius is larger for the coherent reversal model than for the domain wall movement model. For both multilayer samples and alloy I we expect a larger nucleation volume for the strongest island from the model. This contradicts the decrease in nucleation volume for islands with a higher anisotropy as was previously found (Engelen et al., 2010). Compensating for the fact that the switching field is not determined at 0 K does not change this relation as shown in table 3.1.

3.7 Acknowledgements

I would like to thank the group of Professor Thomson at Manchester University, UK for hosting me and for the use of their very nice MOKerr setup as well as discussions about the results. Furthermore I would like to thank the Kitakami lab at Tohoku Universiy in Sendai, Japan for providing us with the $Co_{80}Pt_{20}$ alloyed film (Alloy I). I would also like to thank Enrico Keim from MESA+ and Patrick Grunder from Nanophysics for help with the SEM and STEM images and interpretation of the results.

Chapter 4

Temperature dependent measurements on patterned media

4.1 Introduction

Patterned magnetic media are one of the possible solutions for the superparamagnetic limit that current hard disk technology is approaching. A problem that still needs to be overcome is the large variation in required switching field between elements, known as the switching field distribution (SFD), which is likely caused by an intrinsic anisotropy distribution which is already present in the film before patterning (Shaw et al., 2007; Thomson et al., 2006).

Besides the regular switching field distribution, there is also a thermal switching field distribution (SFD_T) which causes the required switching field of a single element to vary between each measurement due to thermal activation (Engelen et al., 2010).

In previous work, statistical measurements were performed using the anomalous Hall effect (AHE) to determine the thermal switching field distribution and from this, extract the switching field in the absence of thermal fluctuations (H_s^0) and the energy barrier in the absence of an external field (E_0) (de Vries et al., 2013; Engelen et al., 2010). The model previously used does however not take temperature dependent variation in material properties into account.

In this chapter we investigate the temperature dependence of the saturation magnetisation ($M_s(T)$) and effective anisotropy ($K_{\mathrm{eff}}(T)$) of a 20 nm Co/Pt multilayer film by VSM. The film is patterned into an array of islands with a 220 nm diameter and a 600 nm pitch. Temperature dependent anomalous Hall effect (AHE) measurements are used to determine the temperature dependence of the switching field of a single weak and strong island ($H_s(T)$) and the temperature dependence of the distribution SFD_T. These measurements will give us insight in the variation in the prediction of H_s^0 and E_0 caused by the temperature dependence of magnetic material parameters.

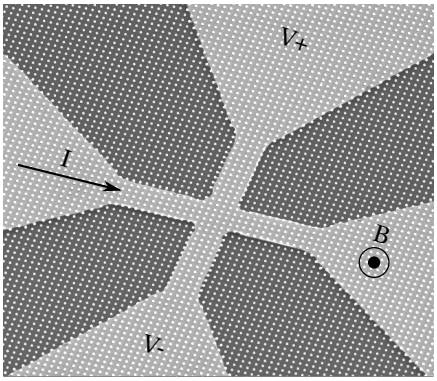

FIGURE 4.1 – *SEM picture of a Hall cross structure with magnetic islands on top, indicating the direction of the current (I), magnetic field (B) and measured Hall voltage (V).*

4.2 Sample description

The sample used for the temperature dependent measurements is the 20 nm multilayer sample which is described in section §3.2.1 and appendix B.

4.3 Theory

4.3.1 Magnetisation and Anisotropy

To determine the temperature dependence of the saturation magnetisation ($M_s(T)$) and the saturation magnetisation at 0 K ($M_s(0)$) a theoretical model should be used. The temperature dependence of the pure cobalt is only 1 % and the largest temperature dependence of the magnetic layer should come from the multilayer (Shan et al., 1994). Since the multilayer consists of a few monolayers per layer, it can then be considered as disordered CoPt and mean field theory can be used (Shan et al., 1993, 1994). This should give an accurate estimation for $M_s(0)$ as a first order approximation.

As the thickness of the Co and Pt are only a few monolayers we assume that the mean field theory should give an accurate prediction. The mean field theory used here is described by Coey (2010) which, using J=2, gives:

$$M_s(T)/M_s(0) = \left(\frac{5}{4}\coth\frac{5}{4}x - \frac{1}{4}\coth\frac{x}{4}\right) \tag{4.1}$$

for the Brillouin function and the equation (Coey, 2010):

$$M_s(T)/M_s(0) = \left(\frac{T}{2T_c}\right)x \tag{4.2}$$

Both functions can be graphically solved, or solved using mathematical software to determine the value of x. Using the measured values of $M_s(T)$ we can determine the value of $M_s(0)$.

To fit the values for the anisotropy we use the same theory as described for the saturation magnetisation. Here we assume that the effective anisotropy consists of two parts, the demagnetising anisotropy $K_d(T)$ which is related to $M_s(T)^2$ as given by the relation $K_d(T) = 0.5\mu_0 M_s(T)^2$ and the uniaxial anisotropy $K_u(T)$ which is related to $M_s(T)^3$ (Asselin et al., 2010). Here the effective anisotropy is given by $K_{eff}(T) = K_u(T) - K_d(T)$. This results in the following equation for the effective anisotropy:

$$\begin{aligned} K_{eff}(T) =& K_u(0)\left(\frac{5}{4}\coth\frac{5}{4}x - \frac{1}{4}\coth\frac{x}{4}\right)^3 \\ & - \frac{1}{2}\mu_0\left(M_s(0)\left(\frac{5}{4}\coth\frac{5}{4}x - \frac{1}{4}\coth\frac{x}{4}\right)\right)^2 \end{aligned} \tag{4.3}$$

4.3.2 Switching field and Energy barrier

The theory in this section closely resembles the theory described in chapter 3. In this section many model parameters are temperature dependent and for clarity all the theory is described again with the temperature dependence.

Statistics

From statistical measurements of the switching field of a single island it is possible to determine the energy barrier in the absence of an external field ($E_0(T)$) and the switching field in the absence of thermal fluctuations ($H_s^0(T)$). The probability that an island has not reversed after time Δt is given by (Engelen et al., 2010; Wernsdorfer et al., 1997):

$$\begin{aligned} P_{\overline{sw}}(\Delta t) &= \exp\left(-\Delta t/\tau\left(H,T\right)\right), \\ \tau\left(H,T\right) &= f_0^{-1}\exp\left(\frac{E_b(H,T)}{k_B T}\right) \end{aligned} \tag{4.4}$$

The probability density is then given by (Wang et al., 2004):

$$\begin{aligned} p_{sw}(H,T) =& \frac{f_0}{R}\exp\left(\frac{-E_b\left(H,T\right)}{k_B T}\right) \\ & \times\exp\left[-\frac{f_0}{R}\int_0^H \exp\left(\frac{-E_b(h,T)}{k_B T}\right)\mathrm{d}h\right] \end{aligned} \tag{4.5}$$

Where the magnetic field is ramped at a rate R, k_B the Boltzmann constant, f_0 is the attempt frequency which is expected to be around 1 GHz (Weller and Moser, 1999) and T the temperature in K. The field dependent energy barrier $E_b(H,T)$, depends in this case on the temperature at which the distribution is measured. This temperature dependence is caused by a variation of the magnetic material properties with temperature.

Energy barrier

For the field and temperature dependent energy barrier we assume two models. The first model is reversal by domain wall movement (appendix C):

$$E_b(H,T) = E_0(T)\left(1 - \frac{H}{H_s^0(T)}\right) \tag{4.6}$$

The value of $E_b(H,T)$ depends here on the applied magnetic field H, the energy barrier in the absence of an external field $E_0(T)$ and the switching field of the measured island $H_s^0(T)$. Both $E_0(T)$ and $H_s^0(T)$ depend on the temperature of the measurement due to the variation of magnetic material parameters with temperature.

Here the nucleation volume can be given by the Barkhausen volume (appendix C):

$$V = \frac{E_0(T)}{2\mu_0 M_s(T) H_s^0(T)} \tag{4.7}$$

The second model is the Stoner-Wohlfarth or coherent rotation model (appendix D):

$$E_b(H,T) = E_0(T)\left(1 - \frac{H}{H_s^0(T)}\right)^2 \tag{4.8}$$

The parameters of both the domain wall and Stoner-Wohlfarth model are the same except for the exponent n, which is 1 for domain wall movement and 2 for Stoner-Wohlfarth. The models will therefore be referred to as "n=1" or "n=2" model.

The nucleation volume for a coherent reversal is given by (appendix D):

$$V = \frac{2E_0(T)}{\mu_0 M_s(T) H_s^0(T)} \tag{4.9}$$

We can use either the coherent reversal or the domain wall movement energy barrier in equation (4.5).

By solving the field H for which $\partial p_{sw}/\partial H = 0$ we can determine the average of the thermal switching field distribution and thus the switching field at the temperature of interest. Using this formula we are able to estimate the nucleation volume for both a weak and a strong island from temperature dependent switching field measurements.

4.4 Experimental

The temperature dependence of the saturation magnetisation ($M_s(T)$) is determined using a VSM. The cooling of the sample is done by a flow of nitrogen

cooling gas. Using a temperature controller the temperature is varied between 170 K and 310 K.

The effective anisotropy is determined at room temperature by a home built torque magnetometer. To determine the temperature dependence of the effective anisotropy the VSM is used in the same temperature range as the saturation magnetisation measurement, from 170 K to 310 K. The VSM measurements are compensated for systematic measurement errors using the measurements from the torque magnetometer.

The anomalous Hall measurement was performed using a different setup than the one used in chapter 3 for the statistical measurements. The system is a modified Oxford VSM with a superconducting magnet. Using a temperature controller and a cryostat, measurements are done between 5 K and 300 K. The magnetic field is applied perpendicular to the sample plane and an AC current at a frequency of 12 333 Hz is used, similar to the measurement from chapter 3. The Hall signal is measured using a lock-in amplifier.

4.5 Results

4.5.1 Saturation magnetisation

The temperature dependent saturation magnetisation is fitted using the combination of equation (4.1) and equation (4.2).

The fitting parameters are the Curie temperature (T_c) and the saturation magnetisation at 0 K ($M_s(0)$). For the errors on the measurement a Monte-Carlo method is used where σ_T=3.5 K and $\sigma_{M_s(T)}$=25 kA m^{-1}. The correct fit should be well within the simulated error. The fitting results and measurement points are shown in figure 4.2.

The Curie temperature is estimated to be 684(58) K. This value is much lower than the value for pure Co (1400 K) but is in the order of other studies on Co/Pt multilayers (van Kesteren and Zeper, 1993; Meng, 1996). The $M_s(0)$ is estimated to be 888(9) kA m^{-1}.

4.5.2 Anisotropy

Equation (4.3) is fitted to the measured $K_{eff}(T)$ with the fit parameters T_c, $M_s(0)$ and $K_u(0)$. The resulting $M_s(0)$ from this fit should not deviate much from the $M_s(0)$ determined in figure 4.2.

For the errors on the measurement a Monte-Carlo method is used where σ_T=3.5 K and $\sigma_{K_{eff}(T)}$=6 kJ m^{-3}.

The $M_s(0)$ is determined to be 863(23) kA m^{-1} which is very close the value of 888(9) kA m^{-1} found from the $M_s(T)$ measurements. K_u is determined to be 889(24) kJ m^{-3} and K_d 468(25) kJ m^{-3}. The value of K_{eff} is estimated to be 421(48) kJ m^{-3}. The fitting value of T_c is in this case 873(20) K.

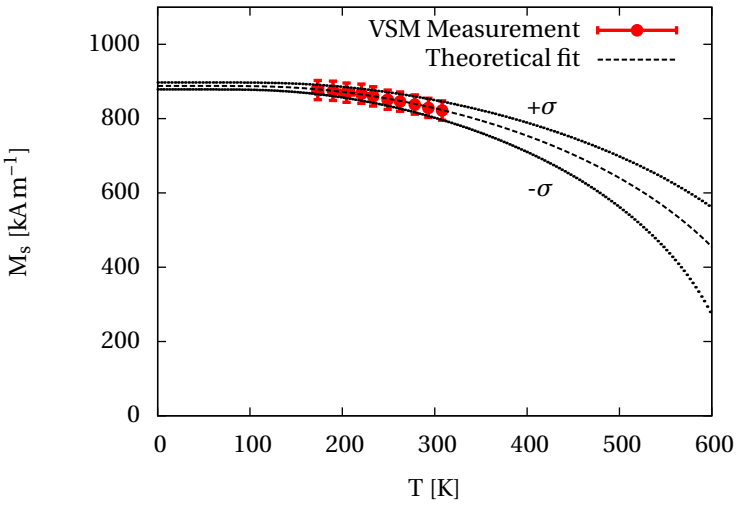

FIGURE 4.2 – *Temperature dependence of M_s from temperature dependent VSM measurements and a fit using equation (4.1) and equation (4.2). The σ lines indicate the 68.2 % confidence interval.*

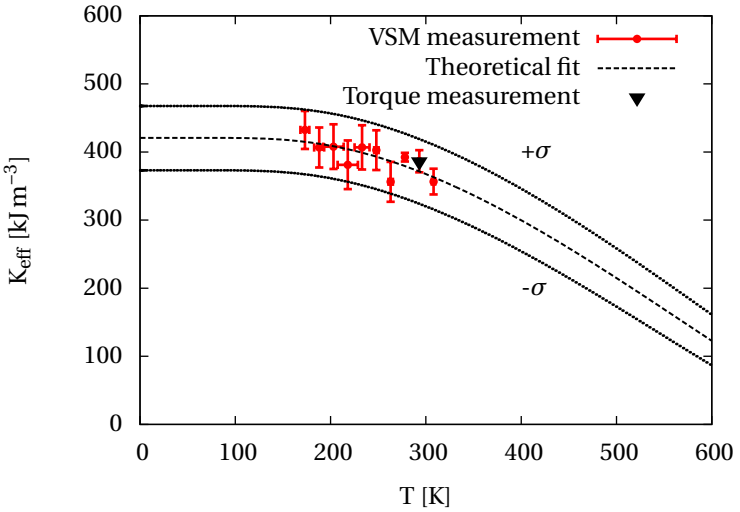

FIGURE 4.3 – *Temperature dependent anisotropy VSM measurements and a torque measurement at room temperature. The theoretical fit is created using equation (4.3). The σ lines indicate the 68.2 % confidence interval.*

4.5.3 Hall measurements

Statistics

The AHE measurement technique is described in section §3.4.3 with a typical measurement with steps corresponding to the reversal of a single island shown in figure 3.4. To determine the statistical distributions at 300 K and 10 K, the switching field of a single weak and a single strong island are measured over 150 times. The temperature variation from the setpoint is less than 0.1 K during switching. Although the weak and strong islands at the two temperatures are in the expected regions, it can not be guaranteed that the weak island at 10 K is the same island as the one at 300 K. For the strong island it is likely that at both temperatures the same island is measured.

The statistical measurement at 300 K has been performed at a field sweep rate R of 39 A m^{-1} s^{-1} and the field sweep rate at 10 K was 3.9 A m^{-1} s^{-1}. The results for both the 10 K and 300 K statistical measurement are shown in figure 4.4.

Figure 4.5 shows the same distributions as figure 4.4 but normalised to the average switching field. As can be seen here, the distribution relative to the switching field at the same temperature is lower for the strong island and the distribution at lower temperatures is smaller for a weak and a strong island.

Equation (4.4) is fitted to both distributions where $E_0(T)$ and $H_s^0(T)$ are the fitting parameters. The results of the fitting parameters of all four fits are given in table 4.1

Temperature dependence

To determine the temperature dependence of the switching field of a single island, the field is swept between sample saturation levels at a constant rate R of 39 A m^{-1} s^{-1}. The temperature is kept constant during the measurement and deviations from the setpoint are less than 0.5 K at the switching event.

To fit the temperature dependent measurements, the theory from equation (4.4) is used together with the energy barriers from equation (4.6) and equation (4.8) for n=1 and n=2. Here the E_0 is replaced by the volumes given in equation (4.7) and equation (4.9) for n=1 and n=2. We assume that the volume is constant and does not vary with temperature. The used fit parameters are the nucleation volume V and the switching field at 0 K, H_s^0. The result of this measurement and the fits are shown in figure 4.6 and table 4.2.

4.6 Discussion

4.6.1 Switching field

Statistics

The distributions of the switching field of a weak and a strong island are measured at 10 K and 300 K. By fitting equation (4.5) using equation (4.8) for co-

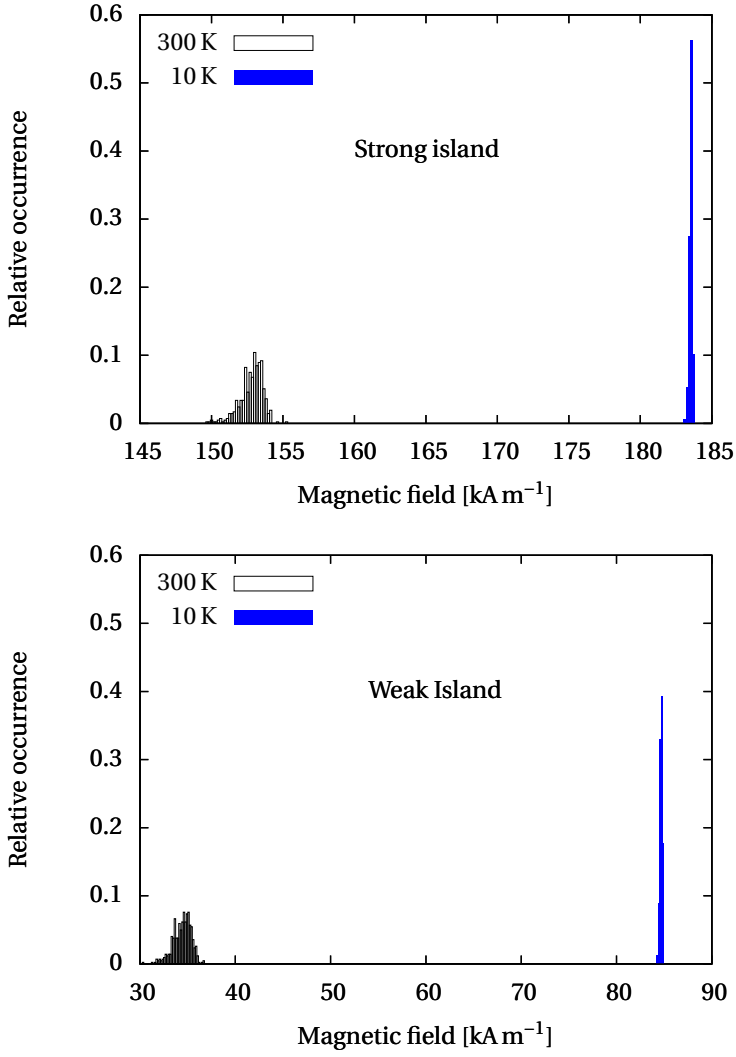

FIGURE 4.4 – *Histograms of the switching field of over 150 reversal incidents of a weak and strong island measured at 10.0(1) K and 300.0(1) K. The bins are normalised to the total amount of reversals, so that the integral under the curves equals one. The width of each bin in the histogram is 0.16 kA m^{-1}*

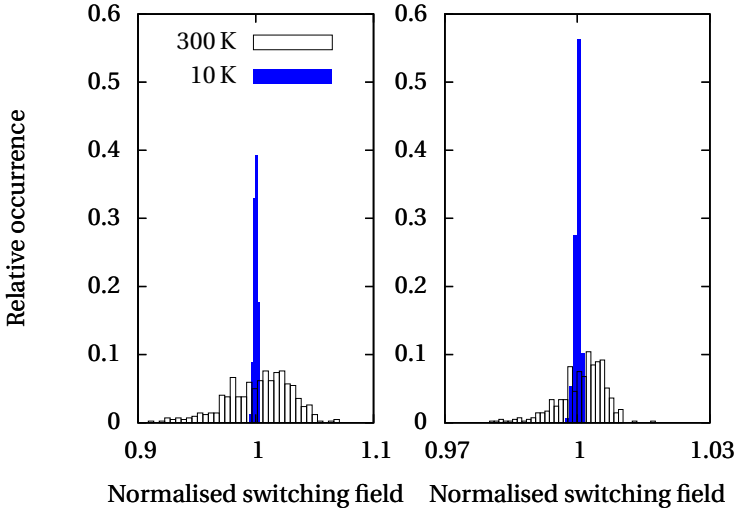

FIGURE 4.5 – *Histograms of the switching field of over 150 reversal incidents of a weak (left) and strong (right) island measured at 10.0(1) K and 300.0(1) K. The bins are normalised to the total amount of reversals, so that the integral under the curves equals one. Both the width of each bin in the histogram and the x-axis value are normalised to the average switching field. The blue bars show the measurement at 10 K and the open boxes show the measurement at 300 K*

.

TABLE 4.1 – *Energy barrier and switching field in the absence of thermal fluctuations determined by statistical measurements of the reversal of a weak and a strong island at 10.0(1) K and 300.0(1) K. It cannot be guaranteed that the weak and strong islands at both temperatures are the same island. The values in parentheses show the 95 % confidence intervals obtained from the fitting algorithm. The magnetic field values are given in kA m^{-1}*

	Weak		Strong	
	1	2	1	2
$H_s^0(300)$ [kA m^{-1}]	53.59(10)	73.65(20)	168.24(08)	184.40(16)
$H_s^0(10)$ [kA m^{-1}]	87.28(03)	90.00(07)	185.51(02)	187.59(03)
$E_0(300)$ [eV]	1.74(01)	2.20(01)	6.74(03)	21.06(18)
$E_0(10)$ [eV]	0.65(01)	5.51(13)	1.78(01)	40.55(49)

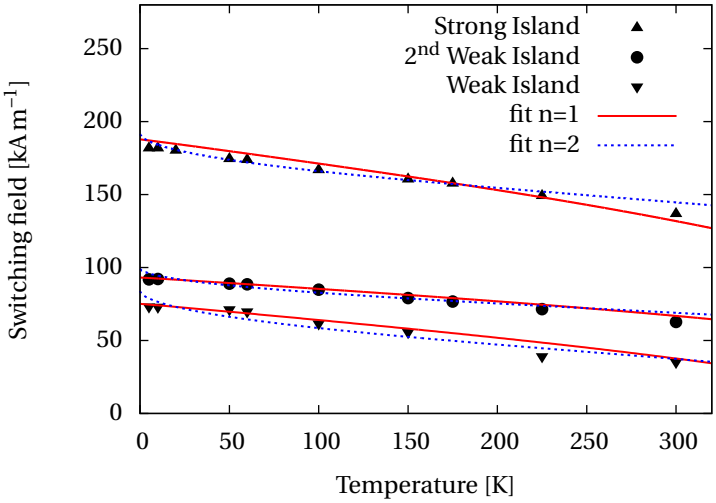

FIGURE 4.6 – *Temperature dependent switching field for two weak and a strong island using temperature dependent AHE measurements. The lines are fitted using equation* (4.5) *with the energy barriers given by equation (4.7) for n=1 and equation (4.9) for n=2. The fit parameters are the nucleation volume V and the switching field at 0 K $H_s(0)$*

TABLE 4.2 – *Theoretical switching field at 0 K and the radius of a cylindrical nucleation volume with a height of 20 nm determined from the fits to the data points in figure 4.6. The energy barriers are determined using equation (4.6) and equation (4.7) for n=1 and equation (4.8) with equation (4.9) for n=2*

	Weak		2nd Weak		Strong	
	n=1	n=2	n=1	n=2	n=1	n=2
H_s^0 [kA m^{-1}]	75.08(02)	84.59(03)	93.14(01)	99.60(06)	183(2)	192.4(4)
radius [nm]	4.60(01)	11.67(11)	5.1(9)	18.07(04)	4.3(3)	16.19(21)
$E_0(0)$ [eV]	1.39(01)	2.50(06)	2.82(70)	7.11(07)	3.01(41)	11.04(36)

herent rotation (n=2) and equation (4.6) for domain wall movement (n=1) we determine $H_s^0(T)$ and $E_0(T)$. The fitting results in table 4.1 show that $H_s^0(10)$ is always higher than $H_s^0(300)$, independent of the reversal model.

This might be explained by the ratio between the increase in K_u and in M_s with decreasing temperature. The increase in K_u from 300 K to the theoretical determined value at 0 K is 16 %, but the increase in M_s is only 7 %. When we look at the relation $H_s^0 = 2K_u/\mu_0 M_s$ we would expect a higher H_s^0 when the statistical measurement is performed at a lower temperature due to the much larger increase in K_u than in M_s.

Temperature dependent

Looking at figure 4.6 we see that for the strong island, the measurement points are on a slightly bigger decline than for the weak island. Although the strong island has a slightly bigger decline than weak island, the temperature dependence of H_s^0 is larger for the weak island than for the strong island due to the large difference in switching field. The decrease in switching field from the theoretical value at 0 K to the measured value at 300 K is 53 % to 58 % for the weak, and 25 % to 29 % for the strong island depending on the reversal mechanism. The temperature dependence of a second weak island with a switching field at 300 K between the weak and the strong island was measured. The decrease in switching field for this second measured weak island is 32 % to 37 %. This is a larger decrease in switching field than the strong island, but a smaller decrease than the weak island. Also the decline of these measurement points is less steep than for both the weak and strong islands.

Temperature dependent vs. statistics

From both statistical and temperature dependent measurements it is clear that the switching field increases with decreasing temperature. By determining the $H_s^0(300)$ by statistical measurements we find the switching field in the absence of thermal fluctuations at 300 K. This result is different from H_s^0 determined by temperature dependent measurements due to the variation in material parameters with the temperature. From this we conclude that, to determine the switching field in the absence of thermal fluctuations, statistical measurements at the temperature of interest should be used. To determine the switching field at 0 K it is necessary to perform temperature dependent measurements.

4.6.2 Energy barrier

Statistics

The relation between E_0 measured at 10 K or at 300 K is not as clear as the relationship for H_s^0 (table 4.1). If we assume a domain wall movement model (n=1) $E_0(10)$ is lower than $E_0(300)$ for both weak and strong islands. However if we assume a coherent rotation model (n=2), we find that $E_0(10)$ is higher

than $E_0(300)$ for both weak and strong islands. A likely cause is that the correct reversal mechanism is neither n=1 nor n=2. This causes the n=1 model to underestimate E_0 and n=2 to overestimate E_0.

Temperature dependent

The energy barriers determined from the temperature dependent switching field measurements (table 4.2) show less variation between the reversal models. For n=1, the value of $E_0(0)$ is similar for both a weak and a strong island. For n=2, $E_0(0)$ of the strong island is 1.5 times higher than that of the weak island whereas the difference determined from statistical measurement is a factor of 3 (300 K) to 23 (10 K). It was however still found that the $E_0(0)$ is always higher for a strong island than for a weak island, independent of the reversal model.

Temperature dependent vs. statistics

To determine the energy barrier from either statistical measurements or temperature dependent measurements a good reversal model is required. Due to the size of the islands it is certain that reversal does not take place by coherent reversal and the domain wall model assumes that domain walls are already present in the islands. To determine the actual value of the E_0 a better reversal model is required, but the result from the n=1 and n=2 models should give a good estimate of the extreme values of the switching field and energy barrier.

4.7 Conclusion

The thermal dependence of the switching field is comparable for a weak and a strong island (figure 4.6). The shape of the distribution is similar for the reversal of each island at 10 K and 300 K and the spread decreases with decreasing temperature, indicating that the spread in switching field is caused by thermal fluctuations and not by reversal order of neighbouring islands.

The saturation magnetisation increases slightly with decreasing temperature. The temperature dependence can be fitted by the mean field theory, leading to an M_s which is 7 % higher at 0 K than at room temperature. The total effective perpendicular anisotropy of the film increases with decreasing temperature, even though the magnetisation, and therefore the demagnetisation, increases. The decrease in effective anisotropy can be fitted to a function where $K_u(T) \sim M_s(T)^3$ and $K_d(T) = 0.5\mu_0 M_s(T)^2$. According to the fit, the effective anisotropy at 0 K is 16 % higher than at room temperature.

From statistical measurements we conclude that the switching field in the absence of thermal fluctuations decreases with temperature. The temperature dependence is more prominent for weak islands (53 % to 58 % decrease from 0 K to 300 K), than for strong islands (25 % to 29 % decrease from 0 K to 300 K) depending on the reversal mechanism. A second weak island, with a switching

field between the weak and strong island, also shows a more prominent temperature dependence than the strong island, but a less prominent temperature dependence than the weak island with a decrease in switching field of 32 % to 37 % from 0 K to 300 K. The fact that the model underestimates the switching field from measurements performed at room temperature can be explained by the relation H_s^0=2$K_u/\mu_0 M_s$ and the fact that the increase in anisotropy is much larger than the increase in saturation magnetisation when decreasing the temperature.

The temperature dependence of the switching field can be accurately fitted assuming a temperature independent nucleation volume. The value of the nucleation volume depends on the reversal model. For domain wall propagation (n=1), the radius of a cylindrical nucleation volume is in the order of 5 nm, for coherent rotation (n=2) it increases to about 11 nm to 18 nm. There is no difference between weak and strong islands.

The energy barriers obtained from fitting to the statistical measurements shows opposite behaviour with temperature, depending on the reversal model that is used. For n=1 (domain wall propagation) the energy barrier increases with increasing temperature by a factor of three, for weak as well as for strong islands. For n=2 (coherent rotation) , the energy barrier reduces with temperature by about a factor two. The prediction of the energy barriers from the temperature dependent measurements are much closer together for the weak and strong islands, than from the value obtained from the statistical measurements.

Chapter 5

A mega- to gigayear storage medium

5.1 Introduction

The human race has achieved many things we consider worth storing. From paintings found in caves as shown in figure 5.1 to pieces currently on display in musea. Whether it is music, art, literature or scientific breakthroughs, people have tried to ensure preservation of information for future generations.

Musea are filled with art and most of the music and movies today are accessible through the internet, but for how long? At some point humanity as we know it will cease to exist (Elwenspoek, 2011) and slowly all our achievements will disappear. Given sufficient time, all memory of humanity will be erased.

To ensure that knowledge about human life is available for many future generations or even future lifeforms we would require a form of data storage suitable for storage at extreme timescales.

There are of course some requirements for such a data storage system. The system should be able to survive for at least the required time without losing its content. The data should be easily decodable and the data carriers should be stored in locations likely to change little over 1 million years to ensure that the data carrier does not end up at the bottom of the ocean after a million years. It is also necessary of course to determine what data is relevant to store. All aspects of such a storage system are combined in a multidisciplinary project called “the human document project” (Manz, 2010).

Although each of these aspects is of vital importance to ensure that the stored data will survive and is recognised as such, in this chapter we will only focus on the fabrication of a data carrier which can survive for over one million years.

To preserve information for future generations, people have stored data in various ways. In recent years the storage capacity has increased tremendously due to the possibilities created by digital information storage. Where in 1956 the IBM 305 RAMAC was capable of storing 5 MB of data using fifty 24” diameter disks, currently 4 TB can be stored on four 3.5” diameter disks. This means a

FIGURE 5.1 – *Cave painting from the El Castillo cave in Spain, estimated to be over 40 000 years old*

decrease of form factor and power consumption while greatly increasing the storage capacity. This increase in capacity has not yet reached its limit (Muraoka and Greaves, 2011). Although there has been a huge increase in storage density, the data longevity is limited to about a decade.

Storage systems like DVD's will not last much longer and tape storage will (if stored in a proper environment) last only several decades. Archival paper is expected to last up to 500 years but only if it is stored in a suitable environment.

A recent long-term data storage system is created by the 'long now foundation' where the information is etched into a substrate and then electroformed in solid nickel (Long Now Foundation, 2013). The resulting disk contains 13 000 pages of information on more than 1500 human languages. A disadvantage of the disk is that its surface is fragile and can easily be scratched so an encasing of the disk is essential for long time survival and repeated readout might damage the surface of the disk.

If we want to store information for much longer timescales none of the above described media will be suitable and a new type of storage medium is required where the longevity of the data is more important than the storage density.

In order to store information for very long timescales, a medium is required which will survive for at least this period and still contain discernible data. We believe that the relevant storage time should be at least 1 million years and at most 1 billion years (Elwenspoek, 2011).

The type of storage medium suitable for these timescales should likely be fabricated especially for this project. There are many types of media which will be suitable, of which the most exotic is DNA based data storage within a living organism which reproduces itself (Petr et al., 2011). We have chosen a disk based storage system because such a system can be created with technology which is already available and will likely be easier recognisable than a data carrier inside a living organism. Although magnetic based data storage is highly suitable for current purposes, its energy barrier is too low to survive for 1 million years. Moreover, the data could be erased or modified by strong magnetic fields.

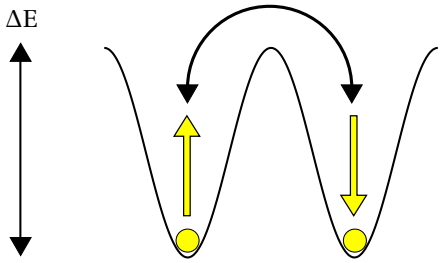

FIGURE 5.2 – *Data is stored in the state of a system, which can be in two or more energy minima.*

We expect that the data that needs to be stored for the Human Document Project will have been thoroughly verified and is not subject to change. Therefore a 'write-once-read-many' (WORM) type data system would be sufficient.

Readback of the disk should be possible using electromagnetic waves which, we expect, any sufficiently developed society would be able to use. The disk can contain multiple levels of data with different data densities. Using visible light the low density data could be read by eye or using optical microscopy. Higher density data could be made visible by for instance electron beams. A dedicated readback system would in this case not be stored with the data carrier because such a system would also need to survive for at least as long as the disk. Plans to create a readback system could be part of the information on the data carrier.

5.2 Theory

All data is volatile so it is not possible to store data indefinitely. Even data engraved in a marble slab will eventually erode away. The longevity of a data carrier can of course be increased by storing it in a monitored environment such as in current paper archives where the humidity, temperature, pressure etc. are controlled. This however, would require that the environment also survives and is maintained for at least as long as the data carrier. We believe that the chances of such an environment surviving for a million years in operating conditions are slim, so we prefer a data carrier which has a high chance of surviving without such a dedicated environment.

In order to create a stable data carrier, able to preserve data for a million years, a high energy barrier against erasure is required. This thermal stability of data is a well studied aspect in magnetic data storage (Charap et al., 1997).

Using a simple but effective theory based on the Arrhenius law, as often used by scientists in the hard disk industry, we can determine the energy barrier required for a certain storage time. For the data storage system we assume that one bit of data is stored in a way much like in current magnetic storage systems. The data is stored in one of the energy minima of the system, which is separated

from the other minima by an energy barrier ΔE, as indicated in figure 5.2. If the system would be kept at a temperature of 0 K, there would be no thermal fluctuations and the system would stay in this state indefinitely. However at elevated temperatures, the probability that the system will jump to another energy minimum after time t, P_{sw} is given by the Arrhenius law (Wernsdorfer et al., 1997).

$$P_{sw} = 1 - \exp\left(-t/\tau\left(T\right)\right)$$
$$\tau\left(T\right) = f_0^{-1} \exp\left(\Delta E/k_B T\right) \tag{5.1}$$

Where τ is the decay time [s], k_B Boltzmann constant [$J K^{-1}$], T the absolute temperature [K] and f_0 the attempt frequency [Hz] which is related to the atomic vibrations and is in the order of 1 GHz for magnetic particles (Weller and Moser, 1999).

We assume that the probability of switching from one of the energy minima to another is low, so we can neglect secondary processes like switching back to the original energy minimum. We also assume that the switching behaviour of one element does not influence the switching behaviour of the others. In this case the number of incorrect bits of information in a large data set of N bits is given by $P_{sw}N$. In modern storage systems error fractions up to α of 1×10^{-5} can be comfortably corrected by suitable error codes. Rewriting equation (5.1) gives:

$$\tau > -t/\ln\left(1-\alpha\right) \approx t/\alpha \qquad \text{for } \alpha \ll 1$$
$$\text{and} \qquad \Delta E/k_B T > \ln\left(t f_0/\alpha\right) \tag{5.2}$$

For a data storage time of 1 million years with α=1×10^{-5} and f_0=1 GHz, ΔE should be 63 $k_B T$, for 1 billion years the energy barrier should be raised to 70 $k_B T$ (1.8 eV at room temperature). These energy barriers are given for the ideal case, where there are no distributions of properties which lower the energy barriers. These values are well within the range of today's technology.

To prove that the data will in fact remain without uncorrectable errors for one million years is another challenge. To wait for a million years to be certain that the data remains would be slightly impracticable, so an accelerated ageing test is required. Starting from equation (5.2) there are three variables we can act upon, the testing time t_t, the observed number of errors during the test α_t and the temperature at which the tests are performed T_t.

$$\Delta E/k_B T_t > \ln(t_t f_0/\alpha_t) \tag{5.3}$$

By observing many bits, we can determine error rates lower than 1×10^{-5} and extrapolate from there when this value will be reached. By testing at higher temperatures, we can increase the number of errors per time unit. Combining equation (5.2) and equation (5.3), the temperature at which the test is performed is given by:

Storage period	1 hour	1 week	1 year
1×10^6 years	461 K	411 K	380 K
1×10^9 years	509 K	455 K	420 K

TABLE 5.1 – *Testing at elevated temperatures to prove data retention for different timescales at T=300 K with α=1 × 10^{-6}*

$$T_t > T \frac{\ln\left(\frac{t f_0}{\alpha}\right)}{\ln\left(\frac{t_t f_0}{\alpha_t}\right)} \tag{5.4}$$

Taking for instance an observed error rate ten times better than the desired rate (so α_t=1 × 10^{-6}), the required testing temperature to prove that the data is stable for a million years within a year is 380 K. Table 5.1 lists values for different testing and storing times, which are well within the experimental range.

This simple model is a first step towards proving that data will be retained for at least one million years by means of an elevated temperature test. This method is also known as accelerated ageing (Zou et al., 1996). The method does have its shortcomings however.

5.2.1 Attempt frequency

The simple Arrhenius model assumes that the attempt frequency to overcome the energy barrier is much higher than the reciprocal of the testing time (in other words, there should be many attempts to switch the entire bit within the testing period). This condition is most likely met. Other causes of data loss, such as theft, meteor impact or the sun entering the red giant phase (Elwenspoek, 2011) cannot be revealed by accelerated ageing (fortunately).

5.2.2 Local minima

The model assumes that one single event switches the bit. Whereas this might be true for patterned magnetic disks, it certainly is not the case for all data storage systems. In the simple model, we assume that the system only possesses global minima, where local minima might exist which can serve as intermediate steps towards overcoming the energy barrier between global minima states. An example of such a system is the phase change medium (used in rewritable optical discs) where data is stored in the position of atoms, which can reside in a huge number of local minima. In this case the chance of switching should be calculated as a cascade of events, each possibly with their own attempt frequency. The process could then be described by an Arrhenius cascade (Bardou, 2000).

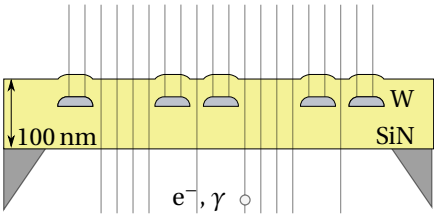

FIGURE 5.3 – *W-Si_3N_4 WORM medium, which is transparent to electron or photon beams*

5.2.3 Temperature dependence

The simple model assumes that the energy barrier is independent of the temperature. In most situations this will not be the case. In general the energy barrier will decrease with increasing temperature. An accelerated test will then underestimate the lifetime of the medium. The model also assumes that attempt frequencies are independent of the temperature. Fortunately, the attempt frequency appears in both the numerator and denominator of equation (5.4). A ten-fold increase in attempt frequency only reduces the temperatures in table 5.1 by 10 K. Detailed knowledge on the attempt frequency is of lesser importance, as is obvious from equation (5.2).

Despite the shortcomings of the single switch Arrhenius model, it is still of interest to perform actual accelerated tests on a real medium, especially at temperatures much higher than listed in table 5.1.

5.3 Fabrication

The suggested data storage system consists of a medium where the data is represented by one material embedded within a second, different material as schematically described in figure 5.3. We have selected as the base materials tungsten for the data and Si_3N_4 for the encapsulating material. Tungsten has a high melting temperature and high activation energy, furthermore it has a low thermal expansion coefficent. The Si_3N_4 has a high fracture toughness and low thermal expansion coefficient. Another important feature of the Si_3N_4 is its transparency to light. A very thin film would also be transparent to electron beams. These materials are readily available and generally used in microfabrication.

An alternative to the transparent medium is a medium with high contrast in reflection. Contrast can be enhanced by using an optical beam of a single wavelength. If the layer thickness is tuned correctly, constructive interference can occur in the parts where there is no metal and destructive interference in the parts where metal is present or vice versa, as shown schematically in figure 5.4. This makes it possible to have a much thicker base because the sample

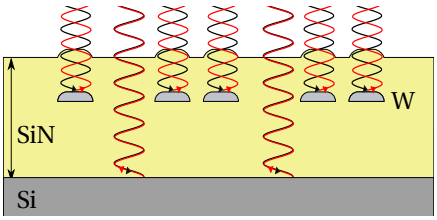

FIGURE 5.4 – *W-Si_3N_4 WORM medium, which is readable by constructive interference on the silicon base and destructive interference on the tungsten islands.*

does not need to be optically transparent. It should however still be ensured that not all the light gets absorbed by the nitride layer. With light in the visible spectrum, this method can be used for low density data.

5.3.1 Optical readable data

As a demonstration, data is written in two-dimensional (matrix) barcodes, which can be read back by a camera and computer. These two-dimensional barcodes were introduced for cases where more information needs to be stored than can be accomodated by their one-dimensional predecessors, but are now becoming increasingly popular. The implementation we chose was the quick response (QR) code (Vongpradhip, 2013), which can be easily decoded by todays smartphones. The level of QR code containing the largest amount of information can lose up to 7 % of the data before the code becomes unreadable.

For the encoding of the final disk, it is likely that a coding scheme would be required which focusses on easy decodability. By keeping the size of the QR code low, it is possible to read out the disk by an optical microscope. For the demonstration, the entire disk was covered with a centimeter sized QR code. Each pixel of the code consists of a set of much smaller QR codes with pixels of only a few micrometers in size as shown in figure 5.5

For design of the thickness of the nitride layers and the tungsten layers, optical calculation software was used in order to determine the optimum thickness for maximum extinction and amplification in the layers. The wavelength was chosen to be 550 nm.

The medium consists of a 338 nm layer of LPCVD Si_3N_4 on a bare silicon wafer. The tungsten is patterned using optical lithography and a mask containing the QR codes. The process is similar to the Hall cross fabrication described in chapter 3. The pattern is etched using Ar ion beam etching and a top layer of PECVD nitride of 225 nm is deposited on top of the tungsten patterns. The process steps are schematically shown in figure 5.6 where the silicon removal in step 8 is not necessary.

FIGURE 5.5 – *Design of the HDP disk. Each pixel in the large QR codes consists of a QR code.*

5.3.2 Line patterns

Because readout by optical microscope means that the data density is low, it is also necessary to have a higher density storage method. The higher data density storage can be achieved by embedding the data in the nitride for readout by electron beam. Here we assume that the medium should be transparent to electrons, which means that the disk will be very thin and fragile.

For the high data density sample, tungsten lines are used instead of islands. With this sample it is possible to simulate high density data with a linewidth below 100 nm.

The lines will make it easier to create very small structures and inspect the sample after thermal exposure by means of an SEM. A drawback of these lines is the variation in stress in the sample in the direction along the lines compared to across the lines. The process steps are described in figure 5.6.

The test sample is created by depositing a layer of 230 nm silicon nitride on a cleaned bare silicon wafer by an LPCVD process. On top of the silicon a layer of 50 nm tungsten is deposited by magnetron sputtering. A layer of DUV 30-J8 bottom anti-reflective coating (BARC) is applied by spin coating, which limits the standing waves in the resist and improves the vertical sidewalls. On top of the BARC, a layer of PEK-500 positive resist is spun.

Laser interference lithography (LIL) is used to create the pattern of 100 nm wide lines (Luttge et al., 2007). For the actual data carrier either a standard lithography mask process could be used or a laser could be used to write the data in the resist. The resist is developed in OPD4262 after exposure. The process flow is depicted in figure 5.6 and a scanning electron micrograph of the developed sample is shown in figure 5.7 a.

A short O_2 reactive ion beam etching (RIBE) step is used to transfer the pattern into the BARC layer. The BARC pattern is transferred into the tungsten layer by argon ion beam milling as can be seen in figure 5.7 b.

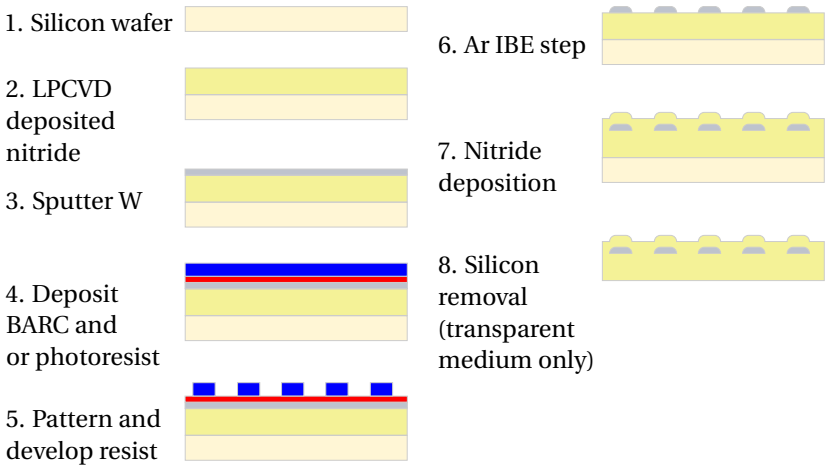

FIGURE 5.6 – *Fabrication process steps for the W-Si_3N_4 test sample*

The entire sample is subsequently covered with Si_3N_4 by a PECVD process to encapsulate the tungsten lines. The result is shown in figure 5.7 c. In the cross-section image from bottom to top, the silicon, the LPCVD silicon-nitride, the tungsten lines and the PECVD silicon nitride can be seen. The Si_3N_4 in the final product is much thicker than the thickness schematically shown in figure 5.3 to observe possible spreading of the tungsten clearly.

For the optical transparent sample, the silicon needs to be removed from the bottom of the sample and a medium with tungsten lines encapsulated in a Si_3N_4 matrix remains. The silicon removal of step 8 shown in figure 5.6 is not performed to ensure mechanical stability of the sample.

5.4 Elevated temperature test

By testing the sample at relevant temperatures it can be shown that it should in principle be possible to store data for at least one million years. A second interesting test would be to investigate whether the sample would survive higher temperatures which would for instance occur during a house fire.

5.4.1 Optical readable data

The sample with the QR codes was exposed to temperatures of 513(5) K, 613(5) K and 713(5) K. Each temperature increase causes a reduction in the number of readable QR codes by the decoding algorithm. This is caused by cracking of the top Si_3N_4 as can be seen in figure 5.8. The unreadable QR codes are not visibly damaged and the tungsten is still present.

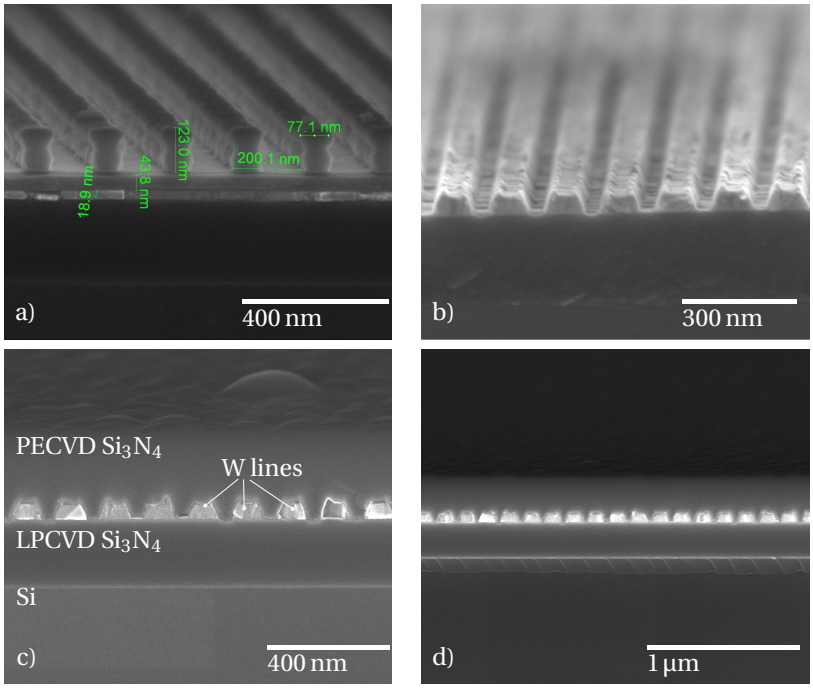

FIGURE 5.7 – *a) Scanning electron micrograph of the test sample before etching. b) Scanning electron micrograph of the test sample after etching containing W lines. c) Scanning electron micrograph of the cross-section of the encapsulated lines in the test sample d) Scanning electron micrograph of the sample after 1 hour at 473 K*

The misreading of the information is caused by the readout using an optical microscope without a monochromatic light source. The images are taken using a top mounted camera and contain a multitude of colours, caused by the variation in Si_3N_4 thickness due to the cracking. The very simple detection software was unable to correctly assign a black or white colour to multitude of colours caused by the cracking of the top siliconnitride layer.

Due to the complexity of the QR code, damage to some areas affects the readability more than other areas (Vongpradhip, 2013). When for instance the finder patterns are damaged, the QR code can not be read anymore. This can be seen from the example in figure 5.9 where the finder patterns of a damaged QR code are manually repaired and the QR code becomes readable again.

A single wavelength microscope or more advanced detection software might solve this problem for the QR codes.

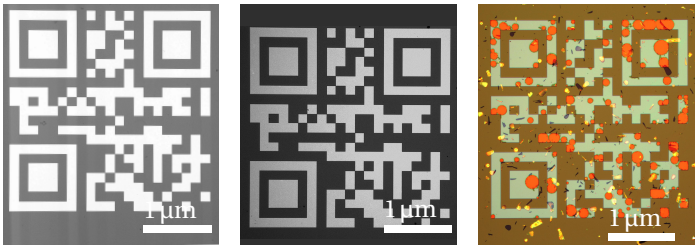

FIGURE 5.8 – *Optical microscope images of the same QR code left: after fabrication, center: after 2 hours at 613 K and right: 2 hours at 763 K*

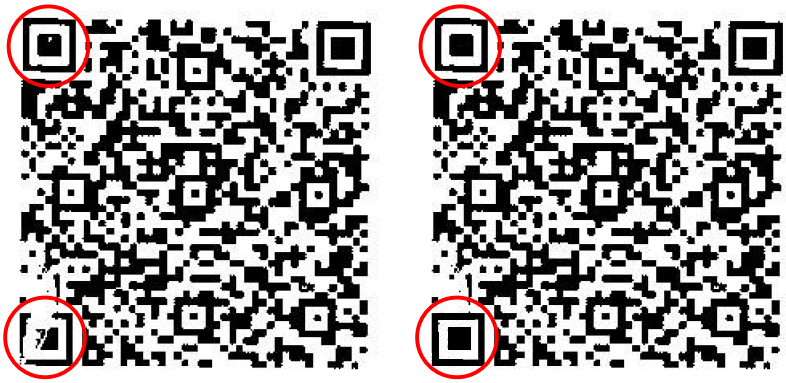

FIGURE 5.9 – *Manually repaired QR codes by fixing the finder patterns in the red circles.*

5.4.2 Line patterns

Table 5.1 shows that an ageing test at 445 K for 1 hour is sufficient to prove that the line sample would survive for at least 1 million years. The sample was kept in an oven at 473 (5)K for approximately one hour. Figure 5.7 c and d show SEM images of the sample before and after the test. We observe no visible degradation of the sample, which indicates that this sample would still be error free after 1 million years. Lower temperatures have not been tested because the PECVD nitride is deposited at temperatures of ~573 K so below this temperature damage would have occured during deposition. The sample has furthermore been tested at 723(5) K and 848(5) K without visible damage to the sample.

A test temperature of 1373(5) K for four hours, which can occur in a hot spot during a house fire, showed that the sample was completely destroyed and the tungsten lines could not be recognised anymore. The Si_3N_4 seems to have peeled off probably due to variations in thermal expansion coefficients of the top and bottom layer Si_3N_4 and the W.

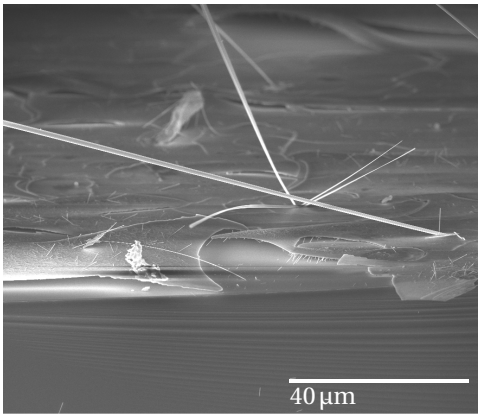

FIGURE 5.10 – *SEM image of the whiskers growing from the top of the sample*

After exposing the sample to a temperature of 923(5) K for 4 hours we observed "whiskers" growing from the top of the sample as can be seen in figure 5.10. Here we also see the peeling of the Si_3N_4 layer. After inspection using an SEM with EDX capabilities we found that the whiskers contain high levels of tungsten and oxygen as can be seen in figure 5.11. What likely has happened is that the top Si_3N_4 deposited by the PECVD process starts to exhibit cracks and oxygen can interact with the tungsten. Under the influence of oxygen and the high temperature, WO whiskers are formed, similar to the ones described by Cho et al. (2004).

Higher temperatures should be possible when the thermal expansion coefficients of the top and bottom layers are matched with the metal layer and the lines are replaced by islands. Previously it was already found that a sample with small dots embedded in Si_3N_4 was able to survive temperatures up to 1073 K for 30 minutes without degradation (Pei et al., 2009). Whether a sample with larger islands would also survive these temperatures remains to be investigated.

5.5 Discussion

The initial attempt to create a medium containing embedded data which is able to survive for 1 million years is promising. The optical readable data in the form of QR codes was able to survive the temperature up to 713(5) K. The amount of readable QR codes decreases at higher temperatures, but this seems to be largely due to the detection scheme as the tungsten is still present. The medium can survive high temperatures, up to 1 hour at 848(5) K, without visible degradation of the medium but at higher temperatures the medium degrades rapidly.

At lower temperatures which corresponds to a storage time of 1 million years or more, the data carrier survives. If we only take the Arrhenius law into account

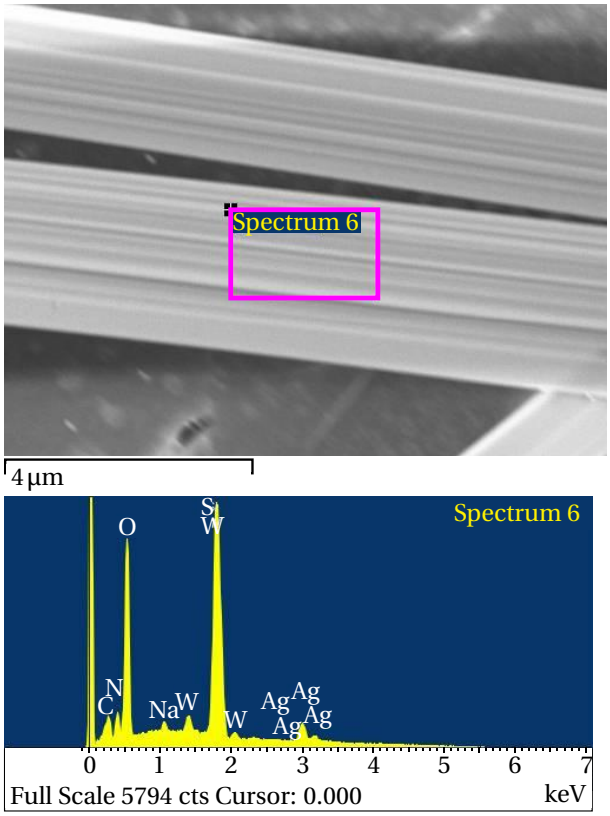

FIGURE 5.11 – *Top: SEM image of the whisker. Bottom: EDX information of the whisker showing large contents of W and O*

this should be sufficient to prove that data will survive for 1 million years.

It is likely however that the Arrhenius law that we use is too simple to describe the real ageing process. If the energy barrier consists of intermediate steps, a cascaded Arrhenius law would be required and data deterioration could occur much faster than expected from these results (Bardou, 2000; Bertin and Bardou, 2008).

We do believe however that diffusion of the tungsten is not the primary concern as shown by the cracks caused by the elevated temperature test. Prolonged exposure of the tungsten to oxygen could lead to the creation of the whiskers. Furthermore low attempt frequency processes like erosion, fracturing and vandalism might have a much larger influence on the lifetime of the disk than diffusion.

The suggested medium is also interesting for fire-proof archiving. Possible solutions to ensure that information could also survive temperatures in the ex-

cess of 973 K to 1173 K would be to have a better encapsulation process ensuring that the thermal expansion coefficients of top and bottom layers are matched with the metal layer. However house fires can contain hot spots with temperatures above 1473 K which might still prove to be too high for the medium to survive. The Si_3N_4 or other encapsulation material should be dense in order to limit the diffusion of oxygen. A different material acting as "data" could also solve the reaction with oxygen. Materials with a slightly lower melting point than the 3683 K of tungsten should be no problem.

When the sample survived a temperature of 848 K for one hour we would, according to the theory, have proven that the sample would last 9×10^{29} years, which is highly unlikely.

5.6 Conclusion

Initial calculations show that it is possible to store data for over 1 million years, or even 1 billion years, with reasonable energy barriers in the order of 70 $k_B T$. To prove that the data will not disappear over this time period, one can perform accelerated ageing tests at moderately elevated temperatures (461 K for 1 hour to represent 1 million years).

A disk with data in the form of QR codes has been fabricated and was able to survive the temperature tests, and therefore will survive one million years of storage according to theory. Data readout failure at even higher temperatures occurs because of the internal stress in the layer stack at elevated temperatures, which leads to fractures in the top layer, resulting in color changes in the readback image.

A model for a high density recording medium, consisting of W lines embedded in a Si_3N_4 matrix has been successfully fabricated. An accelerated ageing test was performed by storing the sample at 473 K for one hour. There was no visible degradation of the sample or the tungsten lines. If we only take diffusion into account this proves that the sample will survive for well over 1 million years when stored at 300 K.

Exposure of the medium to higher temperatures shows degradation due to the difference in thermal expansion coefficients between the two different types of Si_3N_4 and the W lines. The top layer of Si_3N_4 starts to shows cracks and the W is exposed to the environment. This leads to the "whiskers" being grown under the influence of oxygen and high temperature.

5.7 Future work

Reduction of the amount of decodable QR codes is likely caused by the white light source of the microscope and the simple detection scheme. Solving the problem with the variation in stress between the nitride and the tungsten layers would probably also solve the readout issues of the QR codes.

Another influence on the sample could be etching of the nitride due to acids. There are known acids like phosphoric acid which can etch siliconnitride. Also erosion due to influences of for instance wind and sand can deteriorate the medium. A suitable container or storage location can decrease these influences. To properly investigate these influences more advanced tests will have to be performed on the medium.

5.8 Acknowledgements

I would like to thank Kechun Ma and Johnny Sanderink for helping with the fabrication, Mark Smithers for the SEM and EDX measurement and Dimitri Schellenberg for all the work he has done on the QR codes.

Chapter 6

Conclusions

In this thesis I studied the energy barrier which keeps information from being lost in recording media in which every single bit is prepared by lithographic techniques. I studied magnetic media, in which the information is stored in the direction of the magnetisation, as well as write-only media for archival purposes in which the information is stored in the presence or absence of material.

Within a single 350 nm island, multiple energy barriers can be present which need to be overcome to achieve complete magnetisation reversal. The first is the energy barrier preventing nucleation of a reversed domain. Additional energy barriers can be caused by for instance defects in the magnetic layer, leading to domain wall pinning sites. In general the energy barrier of the pinning site is lower than the energy barrier that needs to be overcome to nucleate a reversed domain. This causes the island to completely reverse magnetisation once the reversed domain is formed. In our single 350 nm island, only with an applied field under an angle larger than 85°, the domain wall can be pinned and the required energy barrier to overcome the pinning site is revealed. (Chapter 2)

It was found that an island with a higher switching field also has a higher energy barrier. This is according to expectation, under the assumption that the switching volume and reversal mechanism do not vary considerably for islands with different switching fields. It should be noted however that this finding contradicts earlier work, where an energy barrier independent of the switching field was found. (Chapter 3)

Predictions of the energy barrier by measurements performed at room temperature deviate from the energy barrier determined from temperature dependent measurements. The cause of this deviation is the temperature dependence of magnetic material properties. To determine the energy barrier at room temperature, which is most relevant for application purposes, temperature dependent measurements are not suitable. In this case the statistical measurements can be used to determine the energy barrier at the temperature of interest. (Chapters 3 and 4)

The energy barrier preventing spontaneous reversal of a magnetic island

decreases with increasing temperatures while simultaneously the chance of reversal increases due to thermal excitation. This combination results in a decrease of the average switching field of a single magnetic island with increasing temperature. At the same time the switching field distribution of the single island increases with the increasing temperature. (Chapter 4)

In the second strand of research on thermal activation in data storage, work was carried out to investigate the possibility to fabricate a medium for mega- to gigayear data storage. A medium was succesfully fabricated in which data is stored in tungsten which is encapsulated in siliconnitride. To prove that data will still be readable after one million years or longer, it is necessary to perform a test to overcome the energy barriers preventing data loss at an accelerated rate. This test can be performed at elevated temperatures to increase the chances of overcoming these energy barriers. Assuming an attempt frequency of 1 GHz and error correction, a one hour test performed at temperatures above 473 K shows that the medium will survive for 1 million years or longer. (Chapter 5)

Abbreviations

μSQUID	Superconducting QUantum Interference Device
AC	Alternating Current
AHE	Anomalous Hall Effect
BARC	Bottom Anti-Reflective Coating
BPM	Bit Patterned Media
DC	Direct Current
DNA	DeoxyriboNucleic Acid
DVD	Digital Versatile Disc
EDX	Energy-Dispersive X-ray spectroscopy
FWHM	Full Width at Half Maximum
HAMR	Heat Assisted Magnetic Recording
HDP	Human Document Project
HMDS	HexaMethylDiSilazane
HSQ	Hydrogen SilsesQuioxane
IBE	Ion Beam Etching
LIL	Laser Interference Lithography
LPCVD	Low Pressure Chemical Vapour Deposition
MB	Mega-Byte
Ml	Multilayer
MAMR	Microwave Assisted Magnetic Recording
MFM	Magnetic Force Microscope
MOKE	Magneto-Optic Kerr Effect
OHE	Ordinary Hall Effect
PECVD	Plasma Enhanced Chemical Vapour Deposition
QR	Quick Response
RIBE	Reactive Ion Beam Etching
SEM	Scanning Electron Microscope
SF	Switching Field
SFD	Switching Field Distribution
SFD_T	Temperature dependent Switching Field Distribution
SNR	Signal-to-Noise Ratio
STEM	Scanning Transmission Electron Microscope
TARC	Top Anti-Reflective Coating
TB	Terra-Byte
TEM	Transmission Electron Microscope
TMM	Torque MagnetoMeter

VSM	Vibrating Sample Magnetometer
WORM	Write-Once-Read-Many
XRD	X-Ray Diffraction

Symbols and constants

α	Error fraction
α_t	Error fraction for testing
γ	Photon
θ	Angle between the applied magnetic field and the direction normal to the sample surface in [°]
μ_0	Permeability of vacuum given as $\pi 4 \times 10^{-7}\,\mathrm{V\,s\,A^{-1}\,m^{-1}}$
σ_T	Gaussian error in the temperature used of Monte-Carlo simulations in [K]
$\sigma_{M_\mathrm{s}(T)}$	Gaussian error in the saturation magnetisation used for Monte-Carlo simulations in [$\mathrm{kA\,m^{-1}}$]
$\sigma_{K_\mathrm{eff}(T)}$	Gaussian error in the effective anisotropy used for Monte-Carlo simulations in [$\mathrm{kJ\,m^{-3}}$]
A	Exchange stiffness constant
e^-	Electron
E_0	Energy barrier preventing reversal in the absence of an external field in [eV]
$E_\mathrm{b}(H)$	Field dependent energy barrier preventing reversal in [eV]
$E_0(T)$	Energy barrier in the absence of an external field, determined by statistical measurements at temperature T in [eV]
f_0	Attempt frequency related to the atomic vibration taken as 1 GHz
H	Applied magnetic field in [$\mathrm{kA\,m^{-1}}$]
H_Keff	Effective anisotropy field in [$\mathrm{kA\,m^{-1}}$]
H_n	Nucleation field in [$\mathrm{kA\,m^{-1}}$]
h_p	Pinning field in normalised to H_Keff
H_p	Pinning field in [$\mathrm{kA\,m^{-1}}$]
H_s^0	Switching field in the absence of thermal fluctuations in [$\mathrm{kA\,m^{-1}}$]
$H_\mathrm{s}^0(T)$	Switching field in the absence of thermal fluctuations, determined by statistical measurements at temperature T in [$\mathrm{kA\,m^{-1}}$]
$\mathrm{k_B}$	Boltzmann constant given as $1.38 \times 10^{-23}\,\mathrm{J\,K^{-1}}$
K_d	Demagnetising anisotropy in [$\mathrm{kJ\,m^{-3}}$]
$K_\mathrm{d}(T)$	Temperature dependent demagnetising anisotropy in [$\mathrm{kJ\,m^{-3}}$]
$K_\mathrm{d}(0)$	Theoretically determined demagnetising anisotropy at 0 K in [$\mathrm{kJ\,m^{-3}}$]
K_eff	Effective anisotropy in [$\mathrm{kJ\,m^{-3}}$]
$K_\mathrm{eff}(T)$	Temperature dependent effective anisotropy in [$\mathrm{kJ\,m^{-3}}$]
$K_\mathrm{eff}(0)$	Theoretically determined effective anisotropy at 0 K in [$\mathrm{kJ\,m^{-3}}$]
K_u	Uniaxial anisotropy in [$\mathrm{kJ\,m^{-3}}$]
$K_\mathrm{u}(T)$	Temperature dependent uniaxial anisotropy in [$\mathrm{kJ\,m^{-3}}$]

$K_u(0)$	Theoretically determined uniaxial anisotropy at 0 K in [kJ m^{-3}]
M_s	Saturation magnetisation in [kA m^{-1}]
$M_s(T)$	Temperature dependent saturation magnetisation in [kA m^{-1}]
$M_s(0)$	Theoretically determined saturation magnetisation at 0 K in [kA m^{-1}]
n	The exponent in the energy barrier model, with values 1 for domain wall movement and 2 for Stoner-Wohlfarth reversal
N	Number of bits
p_{sw}	Switching field probability density
R	Field rate given in [kA m^{-1} s^{-1}]
V	Nucleation volume in [m^3]
t	Time in [s]
t_t	Testing time in [s]
T	Temperature in [K]
T_c	Curie temperature in [K]
T_t	Testing temperature in [K]

Appendices

Appendix A

Modified Kondorsky model

To determine the angular dependence of the depinning field in chapter 2 the modified Kondorsky model is used (Schumacher, 1991). The modified Kondorsky model combines the rotation of the magnetisation with the domain wall movement when a magnetic field is applied under an angle.

Using equation (4) from Schumacher (1991) we can write the equilibrium angle with the easy axis as:

$$\psi = \sin^{-1}(h\sin(\theta))$$

with $h = H/(H_a + NM_s)$.

The modification to the normal Kondorsky function is given by equation (6) in the paper as:

$$\frac{\Theta(\theta)}{\Theta(0°)} = h_{//} - \sin^{-1}(h_{//})\cos(\sin^{-1}(h_{//}))$$

With $h_{//} = \cos(\psi)$. Resulting in the modified Kondorsky function (9):

$$F(H_p) = H_p - \frac{H_p(0°)}{\cos(\theta)}\frac{\Theta(\theta)}{\Theta(0°)} = 0$$

The function is solved for the value of h and multiplied by H_{Keff} using mathematical software. This gives the fitting function with the parameters H_{Keff} (which is equal to $H_a + NM_s$) and $h_p(0°)$ which is the pinning field at 0° ($H_p(0°)$) normalised to H_{Keff}.

Appendix B

Process Flow

The multilayer samples described in chapter 3 are also used in chapter 4 and are fabricated using the complete process given in table B. The multilayer samples described in chapter 2 are deposited in the VSW sputtering system and the alloy samples described in chapter 3 are patterned using the LIL steps. The ”alloy I” sample has been etched in the Oxford i300 RIBE system.

For easier readability the important parts of the process are:

- step 2 to 9: Standard wafer cleaning
- step 13: Metal layer deposition
- step 15 to 30: LIL procedure for patterned media
- step 31 to 41: Hall cross fabrication

After etching step 30 it is necessary to remove the remaining BARC and redeposited material which is present on top of the magnetic islands. An adhesive layer (KAPTON foil) is used to peel of the BARC/resputtered material. If this is unsuccessful a mechanical removal step is performed using a cleanroom tissue.

TABLE B.1 – *The fabrication process details.*

	Process		Note
1	Substrate- Silicon ⟨100⟩ OSP	Supplier: Okmetic ◦ Orientation: ⟨100⟩ ◦ Diameter: 100 mm ◦ Thickness: 525 µm ± 25 µm ◦ Polished: Single side (OSP) ◦ Resistivity: 5 MΩ to 10 MΩ ◦ Type: p	
2	Clean HN03-1	NL-CLR-WB14 ◦ Beaker 1: HNO_3 (99%) ◦ Time: 5 min	Steps 2 through 9 are used as the standard cleaning recipe.
3	Clean HN03-2	NL-CLR-WB14 ◦ Beaker 2: HNO_3 (99%) ◦ Time: 5 min	
4	Quick Dump Rinse (QDR)	NL-CLR-WB14 Recipe 1 QDR: 2 cycles of steps 1 to 3, ◦ 1: fill bath 5 s ◦ 2: spray dump 15 s ◦ 3: spray-fill 90 s ◦ 4: end fill 200 s Recipe 2 cascade rinsing: continuous flow untill the DI resistivity is > 10 MΩ	
5	Clean HNO3-3a/b	NL-CLR-WB14 beaker 3a/b: HNO_3 (69%), ◦ temperature 95 °C ◦ time > 10 min	
6	Quick Dump Rinse (QDR)	NL-CLR-Wet benches Recipe 1 QDR: 2 cycles of steps 1 to 3, ◦ 1: fill bath 5 s ◦ 2: spray dump 15 s ◦ 3: spray-fill 90 s ◦ 4: end fill 200 s Recipe 2 cascade rinsing: continuous flow untill the DI resistivity is > 10 MΩ	
7	Etching in HF 1 % (prefurnace)	NL-CLR-WB15 use beaker HF 1 % ◦ time variable ◦ native oxide strip: > 1 min or hydrofobic surface	

TABLE B.1 – *Continued...*

	Process		Note
8	Quick Dump Rinse (QDR)	NL-CLR-Wet benches Recipe 1 QDR: 2 cycles of steps 1 to 3, ◦ 1: fill bath 5 s ◦ 2: spray dump 15 s ◦ 3: spray-fill 90 s ◦ 4: end fill 200 s Recipe 2 cascade rinsing: continuous flow untill the DI resistivity is > 10 MΩ	
9	Substrate drying	NL-CLR-WB Single wafer dryer ◦ Speed: 2500 rpm ◦ Time: 60 s with 30 s N_2 flow	
10	LPCVD of SiO2 (TEOS)	NL-CLR-LPCVD H3 ◦ Program: N2 ◦ TEOS flow: 40 sccm ◦ Bubbler N2 : 30 sccm ◦ temperature: 710 °C (Z1), 725 °C (Z2), 740 °C (Z3) ◦ pressure: 400 mtorr ◦ Stress: 282 MPa ± 13 MPa (after anneal @1150 °C, 3hr) ◦ deposition rate: 8.1 nm min^{-1} (1100 nm) ◦ wafer non-uniformity: 3.6 % ◦ boat non-uniformity: 1.0 % ◦ Nf: 1.434	
12	NL-CLR-Plasmos Ellipsometer		Verify the thickness of the SiO_2 layer.
13	Sputtering of metal layers	VSW sputtering system ◦ Target-sample distance: 10 cm ◦ Ar flow: 10 sccm ◦ Rotation: ON ◦ Tantalum: Pressure 1×10^{-2} mbar Power: 30 W Sputterrate: 0.084 nm s^{-1} ◦ Cobalt: Pressure 8×10^{-3} mbar Power: 30 W Sputterrate: 0.019 nm s^{-1} ◦ Platinum: Pressure 8×10^{-3} mbar Power: 30 W Sputterrate: 0.105 nm s^{-1}	

TABLE B.1 – *Continued...*

	Process		Note
14	XRD measurement		Reflectivity high angle diffraction and rocking curve.
15	Dehydration bake	Hotplate ◦ Temp: 180 °C ◦ Time: 5 min	
16	Spin BARC	SSE Opticoat ST 22+ ◦ 1.5 mL DUV-30 ◦ Recipe: Closed 4000 rpm ◦ Time: 45 s	First layer improves adhesion.
17	BARC bake	Hotplate ◦ Temp: 90 °C ◦ Time: 30 s	
18	BARC bake	Hotplate ◦ Temp: 180 °C ◦ Time: 45 s	
19	Spin BARC	SSE Opticoat ST 22+ ◦ 1.5 mL DUV-30 ◦ Recipe: Open 4000 rpm ◦ Time: 45 s	
20	BARC bake	Hotplate ◦ Temp: 90 °C ◦ Time: 30 s	
21	BARC bake	Hotplate ◦ Temp: 180 °C ◦ Time: 1 min	
22	Spin photoresist	SSE Opticoat ST 22+ ◦ 1.5 mL PEK500 ◦ Recipe: Open 4000 rpm ◦ Time: 45 s	
23	Bake photoresist	Hotplate ◦ Temp: 105 °C ◦ Time: 90 s	
24	Spin TARC	SSE Opticoat ST 22+ ◦ 1.5 mL AQUATAR ◦ Recipe: Open 3500 rpm ◦ Time: 45 s	

TABLE B.1 – *Continued...*

	Process		Note
25	Laser Interference Lithography (LIL)	NL-CLR-LIL Exposure LIL under an angle of 90° Dosage 1.5 mJ	
26	Development	Development of the LIL pattern Post exposure bake ◦ Temp: 105 °C ◦ Time: 90 s Development OPD4262 ◦ Time: 60 s	
27	SEM analysis		Intensity and exposure time are verified by SEM inspection of the developed LIL profile. If the exposure is unsuccessful, cleaning with aceton and return to process step 22 for photoresist spinning.
28	Cutting/dicing	Cutting or dicing of the samples into 1 cm by 1 cm pieces	
29	Etching	Etching in the Oxford i300 RIBE BARC etch step ◦ Rotation: 5 rpm ◦ Angle: 0° ◦ Coolgas: 5 Torr ◦ Neut.: 100 mA ◦ RF: 400 W ◦ Beam: 50 mA ◦ Voltage: 300 V ◦ Acc: 300 V ◦ Beam: 10 sccm O_2 ◦ Etchrate: ≈1.4 nm s^{-1}	Using molybdenum small sample holder.
30	Etching	Etching in the Oxford i300 RIBE Magnetic layer etch step ◦ Rotation: 5 rpm ◦ Angle: 0° ◦ Coolgas: 5 Torr ◦ Neut.: 100 mA ◦ RF: 400 W ◦ Beam: 50 mA ◦ Voltage: 300 V ◦ Acc: 300 V ◦ Beam: 5 sccm Ar ◦ Etching time: > 150 s	Using molybdenum small sample holder.

TABLE B.1 – *Continued...*

	Process		Note
31	Dehydration bake	NL-CLR-WB21/22 dehydration bake at hotplate ◦ temp. 120 °C ◦ time: 5 min	
32	Priming (liquid)	NL-CLR-WB21/22 Primer: HexaMethylDiSilazane (HMDS) use spincoater (program: 4000): ◦ Speed:4000 rpm ◦ Time: 30 s	
33	Coating Olin Oir 906-12	NL-CLR-WB21 Coating: Primus Spinner ◦ olin OIR 906-12 ◦ spin Program: 4000 (4000 rpm, 30 sec) Prebake: hotplate ◦ time 60 s ◦ temp 95 °C	
34	Alignment & exposure Olin 906-12	NL-CLR- EV620 Electronic Vision Group EV620 Mask Aligner ◦ Hg lamp: 12 mW cm^{-2} ◦ exposure time: 3 s	
35	Development Olin OiR resist	NL-CLR-WB21 After exposure Bake : hotplate ◦ Time 60 s ◦ Temp 120 °C development: developer: OPD4262 ◦ Time: 30 s in beaker 1 ◦ Time: 15 s to 30 s in beaker 2	
36	Quick Dump Rinse (QDR)	NL-CLR-Wet benches Recipe 1 QDR: 2 cycles of steps 1 to 3, ◦ 1: fill bath 5 s ◦ 2: spray dump 15 s ◦ 3: spray-fill 90 s ◦ 4: end fill 200 s Recipe 2 cascade rinsing: continuous flow Rinse untill the DI resistivity is > 10 MΩ	
37	Substrate drying	NL-CLR-WB Single wafer dryer ◦ Speed: 2500 rpm ◦ Time: 60 s with 30 s N_2 flow	

TABLE B.1 – *Continued...*

	Process		Note
38	Postbake Olin OiR resist	NL-CLR-WB21 postbake: Hotplate ◦ temp 120 °C ◦ time 10 min	
39	Inspection by optical microscope	NL-CLR- Nikon Microscope ◦ dedicated microscope for lithography inspection	
40	Etching	Etching in the Oxford i300 RIBE Hall cross etch step ◦ Rotation: 5 rpm ◦ Angle: 0° ◦ Coolgas: 5 Torr ◦ Neut.: 100 mA ◦ RF: 400 W ◦ Beam: 50 mA ◦ Voltage: 300 V ◦ Acc: 300 V ◦ Beam: 5 sccm Ar	Using molybdenum small sample holder.
41	Cleaning aceton & IPA (VLSI)	NL-CLR-WB-11 (right side) Removal of organic residue Use ultrasonic bath 2 or 3 ◦ Beaker 1: Aceton VLSI > 10 min ◦ Beaker 2: IPA VLSI > 10 min ◦ Spin drying	

Appendix C

Barkhausen model

The Barkhausen model assumes that there already is a domain wall present in the film, which separates the two domains. For simplicity we assume an infinitely thin domain wall pinned at position $x = 0$ in an energy minimum. We further assume that the domain wall energy has a nominal value of ϵ_0, which drops to ϵ_m over a distance δ to the pinning site, as shown schematically in figure C.1.

Under application of an external field H, the domain with downward magnetisation becomes energetically more favourable and there will be a force on the wall in the positive x direction.

The field at which the wall will depin can be calculated from the variation in energy with the wall position. The total energy is composed of the wall energy and the Zeeman energy,

$$\begin{aligned} E &= \epsilon_w(x) W h - \mu_0 M_\mathrm{s} H W h (x + \mathrm{L}) + \mu_0 M_\mathrm{s} H W h (-x + \mathrm{L}) \\ &= \epsilon_w(x) W h - 2\mu_0 M_\mathrm{s} H W h x \end{aligned}$$

with:

$$\epsilon_\mathrm{w}(x) = \begin{cases} \epsilon_\mathrm{m} + \frac{x}{\delta}(\epsilon_0 - \epsilon_\mathrm{m}) & -\delta \le x \le \delta \\ \epsilon_0 & \text{otherwise} \end{cases}$$

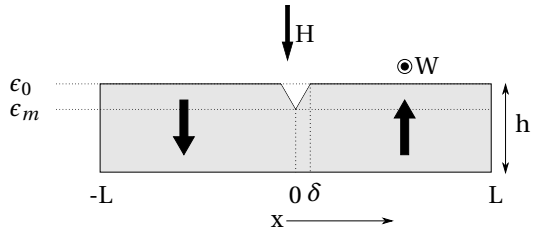

FIGURE C.1 – *Schematic representation of the energy landscape with the pinned domain wall at x=0.*

The energy barrier for domain wall depinning is the difference in energy between the point where the wall has just releases (at $x = \delta$) and the pinned situation ($x = 0$):

$$\begin{aligned}\Delta E &= E(x=\delta) - E(x=0) \\ &= \epsilon_0 W h - 2\mu_0 M_\mathrm{s} H W h \delta - \epsilon_\mathrm{m} W h \\ &= W h \left(\Delta\epsilon - 2\mu_0 M_\mathrm{s} H W h \delta\right) \\ &= W h \Delta\epsilon \left(1 - \frac{2\mu_0 M_\mathrm{s} H W h \delta}{\Delta\epsilon}\right)\end{aligned}$$

with $\Delta\epsilon = \epsilon_0 - \epsilon_\mathrm{m}$.
This can be written as:

$$\Delta E = W h \Delta\epsilon \left(1 - \frac{H}{H_\mathrm{s}^0}\right)$$

with:

$$H_\mathrm{s}^0 = \frac{\Delta\epsilon}{2\mu_0 M_\mathrm{s} \delta}$$

The energy barrier in the absence of an external field is:

$$E_0 = \Delta E(H = 0) = W h \Delta\epsilon$$

Resulting in:

$$\Delta E = E_0 \left(1 - \frac{H}{H_\mathrm{s}^0}\right)$$

The switching volume becomes:

$$V = \frac{E_0}{2\mu_0 M_\mathrm{s} H_\mathrm{s}^0}$$

Appendix D

Stoner-Wohlfarth model

Starting from the energy density for the Stoner-Wohlfarth model as given by Coey (2010) as:

$$E_{\mathrm{SW}} = K_{\mathrm{u}} \sin(\theta)^2 V - \mu_0 M_{\mathrm{s}} H \cos(\alpha - \theta) V$$

As shown schematically in figure D.1. We assume that the angle of the magnetic field with the magnetic easy axis (α) is 90° resulting in:

$$E_{\mathrm{SW}} = K_{\mathrm{u}} \sin(\theta)^2 V - \mu_0 M_{\mathrm{s}} H \sin(\theta) V$$

To determine the height of the energy barrier we take $\partial E_{\mathrm{SW}}/\partial\theta$ and solve it for θ. The height of the energy barrier is at its maximum for:

$$\theta = \cos^{-1}\left(\frac{\mu_0 M_{\mathrm{s}} H}{2K_{\mathrm{u}}}\right)$$

which gives an energy barrier of:

$$E_{\mathrm{SW,max}} = K_{\mathrm{u}} V - \frac{\mu_0^2 M_{\mathrm{s}}^2 H^2 V}{4K_{\mathrm{u}}} - \frac{\mu_0 M_{\mathrm{s}} H V}{K_{\mathrm{u}}}$$

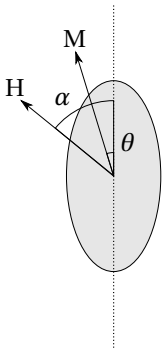

FIGURE D.1 – *Schematic representation of a Stoner-Wohlfarth particle.*

When at zero field ($H = 0$) $E_0 = K_u V$, resulting in:

$$E_{SW,max} = E_0 \left(1 - \frac{\mu_0^2 M_s^2 H^2 V}{4 K_u^2 V} - \frac{\mu_0 M_s H V}{K_u V} \right)$$

Taking:

$$H_s^0 = \frac{2 K_u}{M_s \mu_0}$$

This results in:

$$\begin{aligned} E_{SW,max} &= E_0 \left(1 - \frac{\mu_0^2 M_s^2}{4 K_u^2} H^2 - \frac{\mu_0 M_s}{K_u} H \right) \\ &= E_0 \left(1 - \frac{1}{(H_s^0)^2} H^2 - \frac{1}{H_s^0} H \right) \\ &= E_0 \left(1 - \frac{H}{H_s^0} \right)^2 \end{aligned}$$

The relation between the energy barrier and the switching volume can now be given by:

$$V = \frac{E_0}{K_u} = \frac{2 E_0}{\mu_0 M_s H_s^0}$$

Bibliography

Alexandrou M, 2010
Magneto-optic Kerr and Hall effect measurements for the characterisation of bit patterned media
Ph.D. thesis, The University of Manchester - Faculty of Engineering and Physical Sciences

Alexandrou M, Nutter P W, Delalande M, de Vries J, Hill E W, Schedin F, Abelmann L, Thomson T, 2010
"Spatial sensitivity mapping of Hall crosses using patterned magnetic nanostructures"
J. Appl. Phys. **108**, pp. 043920–1–5, doi: 10.1063/1.3475485

Asselin P, Evans R F L, Barker J, Chantrell R W, Yanes R, Chubykalo-Fesenko O, Hinzke D, Nowak U, 2010
"Constrained Monte Carlo method and calculation of the temperature dependence of magnetic anisotropy"
Phys. Rev. B **82**, p. 054415, doi: 10.1103/PhysRevB.82.054415

Bardou F, 2000
"Cooling gases with Lévy flights: using the generalized central limit theorem in physics"
ArXiv Physics e-prints URL `http://arxiv.org/abs/physics/0012049v1`

Belle B D, Schedin F, Pilet N, Ashworth T V, Hill E W, Nutter P W, Hug H J, Miles J J, 2007
"High resolution magnetic force microscopy study of e-beam lithography patterned Co/Pt nanodots"
J. Appl. Phys. **101**, p. 09F517, doi: 10.1063/1.2713429

Bertin E, Bardou F, 2008
"From laser cooling to aging: A unified Lévy flight description"
Am. J. Phys. **76**, pp. 630–636, doi: 10.1119/1.2888543

Canedy C L, Li X W, Xiao G, 2000
"Large magnetic moment enhancement and extraordinary Hall effect in Co/Pt superlattices"
Phys. Rev. B **62**, pp. 508–519, doi: 10.1103/PhysRevB.62.508

Cayssol F, Ravelosona D, Wunderlich J, Chappert C, Mathet V, Jamet J P, Ferré J, 2002
"Detection of domain wall propagation in a mesoscopic wire"
J. Magn. Magn. Mater. **240**, pp. 30–33, doi: 10.1016/S0304-8853(01)00720-X

Charap S H, Lu P L, He Y, 1997
"Thermal stability of recorded information at high densities"
IEEE Trans. Magn. **33**, pp. 978–983, doi: 10.1109/20.560142

Cho M H, Park S A, Yang K D, Lyo I W, Jeong K, Kang S K, Ko D H, Kwon K W, Ku J H, Choi S Y, Shin H J, 2004
"Evolution of tungsten-oxide whiskers synthesized by a rapid thermal-annealing treatment"
J. Vac. Sci. Technol. B **22**, pp. 1084–1087, doi: 10.1116/1.1738670

Chou S Y, Wei M S, Krauss P R, Fischer P B, 1994
"Single-domain magnetic pillar array of 35 nm diameter and 65 Gbits/in.^{2} density for ultrahigh density quantum magnetic storage"
J. Appl. Phys. **76**, pp. 6673–6675, doi: 10.1063/1.358164

Coey J M D, 2010
Magnetism and magnetic materials,
Cambridge University Press

Delalande M, de Vries J, Abelmann L, Lodder J C, 2012
"Measurement of the nucleation and domain depinning field in a single Co/Pt multilayer dot by Anomalous Hall effect"
J. Magn. Magn. Mater. **324**, pp. 1277–1280, doi: 10.1016/j.jmmm.2011.09.037

Elwenspoek M C, 2011
"Long-time data storage: relevant time scales"
Challenges **2**, pp. 19–36, doi: 10.3390/challe2010019

Engelen J B C, Delalande M, le Fèbre A J, Bolhuis T, Shimatsu T, Kikuchi N, Abelmann L, Lodder J C, 2010
"Thermally induced switching field distribution of a single CoPt dot in a large array"
Nanotechnol. **21**, p. 035703, doi: 10.1088/0957-4484/21/3/035703

Gaunt P, 1986
"Magnetic viscosity and thermal activation energy"
J. Appl. Phys. **59**, pp. 4129–4132, doi: 10.1063/1.336671

Hauet T, Hellwig O, Park S H, Beigné C, Dobisz E, Terris B D, Ravelosona D, 2011
"Influence of ion irradiation on switching field and switching field distribution in arrays of Co/Pd-based bit pattern media"
Appl. Phys. Lett. **98**, p. 172506, doi: 10.1063/1.3581896

van Kesteren H W, Zeper W B, 1993
"Controlling the Curie temperature of Co/Pt multilayer magneto-optical recording media"
J. Magn. Magn. Mater. **120**, pp. 271–273, doi: 10.1016/0304-8853(93)91339-9

Kryder M H, Gage E C, Mcdaniel T W, Challener W A, Rottmayer R E, Ju G, Hsia Y r, Erden M F, 2008
"Heat assisted magnetic recording"
Proc. IEEE **96**, pp. 1810–1835, doi: 10.1109/JPROC.2008.2004315

Lambert C H, Rajanikanth A, Hauet T, Mangin S, Fullerton E E, Andrieu S, 2013
"Quantifying perpendicular magnetic anisotropy at the Fe-MgO(001) interface"
Appl. Phys. Lett. **102**, p. 122410, doi: 10.1063/1.4798291

Lau J W, McMichael R D, Chung S H, Rantschler J O, Parekh V, Litvinov D, 2008
"Microstructural origin of switching field distribution in patterned CoPd multilayer nanodots"
Appl. Phys. Lett. **92**, p. 012506, doi: 10.1063/1.2822439

Long Now Foundation, 2013
URL `http://longnow.org/`

Luttge R, van Wolferen H A G M, Abelmann L, 2007
"Laser interferometric nanolithography using a new positive chemical amplified resist"
J. Vac. Sci. Technol. B **25**, pp. 2476–2480, doi: 10.1116/1.2800328

Manz A, 2010
"The human document project and challenges"
Challenges **1**, pp. 3–4, doi: 10.3390/challe1010003

Meng Q, 1996
Magneto-optical recording media CoNi/Pt and Co/Pt multilayers
Ph.D. thesis, University of Twente

Moser A, Takano K, Margulies D T, Albrecht M, Sonobe Y, Ikeda Y, Sun S, Fullerton E E, 2002
"Magnetic recording: Advancing into the future"
J. Phys. D: Appl. Phys. **35**, pp. R157–R167, doi: 10.1088/0022-3727/35/19/201

Muraoka H, Greaves S J, 2011
"Statistical modeling of write error rates in bit patterned media for 10 tb/in^2 recording"
IEEE Trans. Magn. **47**, pp. 26–34, doi: 10.1109/TMAG.2010.2080354

Neél L, 1949
"Théorie du trainage magnétique des ferromagnétiques en grains fins avec applications aux terres cuites"
Ann. Geophys. **5**, pp. 99–136

Pei Y, Yin C, Nishijima M, Kojima T, Fukushima T, Tanaka T, Koyanagi M, 2009
"Formation of high density tungsten nanodots embedded in silicon nitride for nonvolatile memory application"
Appl. Phys. Lett. **94**, p. 063108, doi: 10.1063/1.3081042

Petr J, Ranc V, Maier V, Ginterová P, Znaleziona J, Knob R, Avek J, 2011
"How to preserve documents: A short meditation on three themes"
Challenges **2**, pp. 37–42, doi: 10.3390/challe2010037

Qin G W, Ren Y P, Xiao N, Yang B, Zuo L, Oikawa K, 2009
"Development of high density magnetic recording media for hard disk drives: Materials science issues and challenges"
Int. Mater. Rev. **54**, pp. 157–179, doi: 10.1179/174328009X411172

Schumacher F, 1991
"On the modification of the Kondorsky function"
J. Appl. Phys. **70**, p. 3184, doi: 10.1063/1.349301

Shan Z S, Nafis S, Woollam J, Liou S H, Sellmyer D J, 1993
"Interface magnetism and superparamagnetism of Co/Cu multilayers"
J. Appl. Phys. **73**, pp. 6347–6349, doi: 10.1063/1.352644

Shan Z S, Shen J X, Kirby R D, Sellmyer D J, Wang Y J, 1994
"Temperature-dependent interface magnetism and magnetization reversal in Co/Pt multilayers"
J. Appl. Phys. **75**, pp. 6418–6420, doi: 10.1063/1.355370

Sharrock M P, McKinney J T, 1981
"Kinetic effects in coercivity measurements"
IEEE Trans. Magn. **17**, pp. 3020–3022, doi: 10.1109/TMAG.1981.1061755

Shaw J M, Rippard W H, Russek S E, Reith T, Falco C M, 2007
"Origins of switching field distributions in perpendicular magnetic nanodot arrays"
J. Appl. Phys. **101**, p. 023909, doi: 10.1063/1.2431399

Shaw J M, Russek S E, Thomson T, Donahue M J, Terris B D, Hellwig O, Dobisz E, Schneider M L, 2008
"Reversal mechanisms in perpendicularly magnetized nanostructures"
Phys. Rev. B **78**, pp. 024414–1–5, doi: 10.1103/PhysRevB.78.024414

Sinitsyn N A, 2008
"Semiclassical theories of the anomalous Hall effect"
J. Phys. Condens. Matter. **20**, p. 023201, doi: 10.1088/0953-8984/20/02/023201

Terris B D, Thomson T, 2005
"Nanofabricated and self-assembled magnetic structures as data storage media"
J. Phys. D: Appl. Phys. **38**, pp. R199–R222, doi: 10.1088/0022-3727/38/12/R01

Terris B D, Thomson T, Hu G, 2007
"Patterned media for future magnetic data storage"
Microsyst. Technol. **13**, pp. 189–196, doi: 10.1007/s00542-006-0144-9

Thomson T, Hu G, Terris B D, 2006
"Intrinsic distribution of magnetic anisotropy in thin films probed by patterned nanostructures"
Phys. Rev. Lett. **96**, p. 257204, doi: 10.1103/PhysRevLett.96.257204

Uesaka Y, Nakatani Y, Hayashi N, 1995
"Switching of single hexagonal particles with nonuniform magnetic properties"
Jpn. J. Appl. Phys. **34**, pp. 6056–6062, doi: 10.1109/20.364584

Victora R H, 1989
"Predicted time dependence of the switching field for magnetic materials"
Phys. Rev. Lett. **63**, pp. 457–460, doi: 10.1103/PhysRevLett.63.457

Vongpradhip S, 2013
"Use multiplexing to increase information in QR code"
In: *8th International Conference on Computer Science and Education, ICCSE 2013*, pp. 361–364, Colombo, doi: 10.1109/ICCSE.2013.6553938

de Vries J, Bolhuis T, Abelmann L, 2013
"Energy barrier versus switching field for patterned $Co_{80}Pt_{20}$ alloy and Co/Pt multilayer films"
J. Appl. Phys. **113**, pp. 17B910–1–17B910–3, doi: 10.1063/1.4801399

Wang H T, Chui S T, Oriade A, Shi J, 2004
"Temperature dependence of the fluctuation of the switching field in small magnetic structures"
Phys. Rev. B **69**, p. 064417, doi: 10.1103/PhysRevB.69.064417

Wang X, Gao K, Zhou H, Itagi A, Seigler M, Gage E, 2013
"HAMR recording limitations and extendibility"
IEEE Trans. Magn. **49**, pp. 686–692, doi: 10.1109/TMAG.2012.2221689

Weller D, Moser A, 1999
"Thermal effect limits in ultrahigh-density magnetic recording"
IEEE Trans. Magn. **35**, pp. 4423–4439, doi: 10.1109/20.809134

Wernsdorfer W, Bonet Orozco E, Hasselbach K, Benoit A, Barbara B, Demoncy N, Loiseau A, Pascard H, Mailly D, 1997
"Experimental evidence of the Néel-Brown model of magnetization reversal"
Phys. Rev. Lett. **78**, p. 1791, doi: 10.1103/PhysRevLett.78.1791

Wu A Q, Kubota Y, Klemmer T, Rausch T, Peng C, Peng Y, Karns D, Zhu X, Ding Y, Chang E K C, Zhao Y, Zhou H, Gao K, Thiele J U, Seigler M, Ju G, Gage E, 2013
"HAMR areal density demonstration of 1+ tbpsi on spinstand"
IEEE Trans. Magn. **49**, pp. 779–782, doi: 10.1109/TMAG.2012.2219513

Zeper W B, Van Kesteren H W, Jacobs B A J, Spruit J H M, Carcia P F, 1991
"Hysteresis, microstructure, and magneto-optical recording in Co/Pt and Co/Pd multilayers"
J. Appl. Phys. **70**, pp. 2264–2271, doi: 10.1063/1.349419

Zhu J G, Zhu X, Tang Y, 2008
"Microwave assisted magnetic recording"
IEEE Trans. Magn. **44**, pp. 125–131, doi: 10.1109/TMAG.2007.911031

Zou X, Uesaka T, Gurnagul N, 1996
"Prediction of paper permanence by accelerated aging I. Kinetic analysis of the aging process"
Cellulose **3**, pp. 243–267, doi: 10.1007/BF02228805

Summary

The key to successful data storage is ensuring that the information is not lost. For thousands of years humankind has stored information, from engravings in marble to magnetic data storage in current times. To ensure the stability of the stored data, an energy barrier is required which separates information from non-information. In marble the energy barrier is caused by the attractive force between atoms and in magnetism it is due to the magnetic anisotropy.

Current hard disk technology has the capability of storing huge amounts of information. A future replacement to the current hard disk is bit patterned media which will make even larger storage capacities possible. In bit patterned media a bit consists of a magnetic island, separated by non-magnetic material. When a magnetic field is applied, which is sufficiently large to overcome the energy barrier, the magnetisation direction will reverse and the bit is written.

Because of differences in these energy barriers, there is a variation between islands in the strength of the magnetic field required to reverse the magnetisation direction. This phenomenon is known as the switching field distribution.

It is possible that there are multiple energy barriers which prevent the complete reversal of the magnetisation. In chapter 2 a situation where multiple energy barriers exist is investigated by applying a magnetic field under an angle with the magnetic easy axis.

Due to the fact that thermal activation aids in overcoming the energy barrier, the required field for reversal varies from instance to instance for the same island. This thermally induced switching field distribution can be used to determine the difference in energy barrier of magnetically weak and strong islands. In chapter 3 an alloy as well as two multilayer structures are compared using this method. In chapter 4 the temperature dependence of the thermally induced switching field distribution is investigated.

For archival purposes it is not the data capacity but the longevity of the data which is most relevant. When we want store information which will outlast the human race, the medium will have different requirements than a medium used for everyday information storage. For a hard disk, a minimum required storage time of 10 years is acceptable, but for such an archival storage system, 1 million to 1 billion years is the relevant timescale. In chapter 5 a storage system has been investigated with high energy barriers which should make data storage for such timescales possible.

Samenvatting

De sleutel tot succesvolle informatie opslag, is ervoor zorgen dat de informatie niet verloren gaat. Al duizenden jaren slaat de mensheid informatie op, van gravures in marmer tot magnetische data opslag in de huidige tijd. Om de stabiliteit van de data te waarborgen is de aanwezigheid van een energie barrière nodig, die de informatie scheidt van de non-informatie. In het marmer is dit de kracht tussen de atomen en in magnetisme is dit de magnetische anisotropie.

Huidige harde schijven hebben de mogelijkheid om enorme hoeveelheden data op te slaan. Een toekomstige opvolger voor de huidige harde schijf technologie, die een nog grotere informatie opslag capaciteit mogelijk maakt, is bit patterned media. Hier bestaat een bit uit een magnetisch eiland omringd door non-magnetisch materiaal. Wanneer er een magnetisch veld aangebracht wordt dat voldoende is om de energie barrière te overwinnen, dan zal de magnetisatie richting omkeren en wordt de bit geschreven.

Door verschillen in deze energie barrières heeft elk eiland een magnetisch veld van een andere sterkte nodig om van magnetisatie richting om te keren. Dit fenomeen is bekend als de switching field distributie.

Het is mogelijk dat er meerdere energie barrières aanwezig zijn, die het volledig omkeren van de magnetisatie verhinderen. In hoofdstuk 2 is een situatie met meerdere energie barrières onderzocht door het aanleggen van een veld onder een hoek met de voorkeursrichting van de magnetisatie.

Aangezien het overwinnen van de energie barrière geholpen wordt door thermische activatie, verschilt het benodigde veld per meting voor hetzelfde eiland. Deze distributie kan gebruikt worden om de energie barrières van magnetisch zwakke en sterke eilanden te bepalen en te vergelijken. Dit gebeurt voor zowel een legering als twee multilaag structuren in hoofdstuk 3. In hoofdstuk 4 wordt de temperatuur afhankelijkheid van deze metingen onderzocht.

Voor archief doeleinden is het niet zozeer de opslag capaciteit maar de levensduur van de informatie die belangrijk is. Wanneer we informatie op willen slaan die langer zal bestaan dan de mensheid zelf, dan gelden er andere eisen dan voor een medium voor dagelijkse informatie opslag. Voor een harde schijf is een minimale opslag tijd van 10 jaar acceptabel, maar voor een dergelijk archief opslag medium is 1 miljoen tot 1 miljard jaar relevant. In hoofdstuk 5 is onderzoek gedaan naar een opslag systeem met hoge energie barrières die opslag voor deze periodes mogelijk maakt.

Acknowledgements

Het is moeilijk om iedereen te bedanken en vooral niemand te vergeten, maar ik zal mijn best doen.

Natuurlijk Peggy die mij enorm gesteund heeft tijdens het promotie onderzoek en er altijd vertrouwen in heeft gehad dat ik het met goed gevolg af zou ronden. Het proefschrift is af, nu het huis nog.

Mijn ouders die gedurende mijn hele studie achter me hebben gestaan en altijd veel begrip hebben gehad. Wendy, Jacco, Nathalie, Pieter, Peggy's ouders, Linda, Paul en Mark voor hun interesse in het toch moeilijke onderwerp.

Natuurlijk bedankt Leon, voor de mogelijkheid om een promotie onderzoek te doen. Ik heb veel geleerd de afgelopen 4 jaar en ik kon altijd makkelijk bij je binnen stappen met vragen of om te overleggen. Daarnaast hadden we natuurlijk ook veel lol op de conferenties, zoals wegrennen voor een tsunami in Matsushima (een jaartje te vroeg) en Cheeseborgers (jawel, met een o) eten in een "restaurantje" in Chicago waar je al dan niet aangerand kon worden op het toilet. Leon, bedankt voor alles en wellicht tot ziens, magnetisme schijnt nu eenmaal een aantrekkingskracht te hebben.

Miko bedankt dat je mijn promotor wilde zijn en voor het doorlezen van het proefschrift en alle tips. De workshop van het "Human Document Project" op Stanford met Egyptologen en Antropologen was erg leuk en ik hoop dat het project een vlucht gaat nemen.

Cock bedankt voor alle tips en de interesse in de stand van zaken wanneer je weer eens op de UT was.

Laurens bedankt voor de mogelijkheid om te overleggen over magnetische data opslag en voor het intensief gebruiken van de patterned media. Je kunt me natuurlijk altijd wakker maken als je hulp nodig hebt met een abstract (is het wel verstandig om dit te zeggen?).

Natuurlijk alle kamer genoten die ik op de 5(!) verschillende kamers heb gehad. Michael voor de spoedintroductie tot patterned media, Johan, Wabe, Shahina en uiteindelijk Rolf en Kodai voor de discussies en gezelligheid.

Thijs bedankt voor alle moeite die je gestopt hebt in de Hall meetopstellingen. Anomalous Hall effect op 5 K is gewoon cool! Martin bedankt voor alle hulp om nog betere MFM plaatjes te maken. Johnny en Henk bedankt voor alle SEM foto's. Henk natuurlijk ook bedankt voor de LIL patronen, ook al weet ik dat maandag, dinsdag, woensdag, donderdag en vrijdag geen goede dagen zijn

voor de LIL (weekenden waarschijnlijk ook niet). Remco bedankt voor het vertrouwen dat ik het lab niet af zou branden met de oven testen. Meint en Erwin bedankt voor het overleggen over de cleanroom proces stappen. Kees bedankt voor alle hulp in de cleanroom. Rico en Mark bedankt voor het TEM, STEM en SEM werk en advies.

My short stay in Manchester was both fun and useful. I would not have guessed that a week would be enough, but we even had time to measure additional samples. Thank you Tom and Paul for hosting me and for the help and advice. Thank you Smaragda, I think I kept you from your own work the entire week and made you get up early.

Kikuchi-san thank you very much for providing us with the alloy sample which proved to be very useful and yielded great results.

De studenten met wie ik samengewerkt heb, Dirk-Jan bedankt voor je enthousiasme en succes met je promotie. Lars pas op met chemicaliën, vooral als Thijs in de buurt is. Dimitri, de QR codes waren een groot succes, wie weet leest iemand ze nog eens over een miljoen jaar ofzo.

Daarnaast kan ik de paranimfen Maaike en Michel natuurlijk niet vergeten. Bedankt dat jullie mijn paranimfen wilden zijn en bedankt voor alle taken die jullie verricht hebben.

Uiteraard bedankt alle mensen van de vakgroep, zowel de vaste staf, Postdocs, AIO's als studenten die er allemaal voor zorgen dat TST een gezellige vakgroep is.

And last but certainly not least, thanks to all the committee members for reading the thesis thoroughly and providing suggestions.

Publications

Journal articles

Alexandrou M, Nutter P W, Delalande M, de Vries J, Hill E W, Schedin F, Abelmann L, Thomson T, 2010
"Spatial sensitivity mapping of Hall crosses using patterned magnetic nanostructures"
J. Appl. Phys. **108**, pp. 043920–1–5, doi: 10.1063/1.3475485

Alink L, Groenland J P J, de Vries J, Abelmann L, 2012
"Determination of bit patterned media noise based on island perimeter fluctuations"
IEEE Trans. Magn. **48**, pp. 4574–4577, doi: 10.1109/TMAG.2012.2201138

Delalande M, de Vries J, Abelmann L, Lodder J C, 2012
"Measurement of the nucleation and domain depinning field in a single Co/Pt multilayer dot by Anomalous Hall effect"
J. Magn. Magn. Mater. **324**, pp. 1277–1280, doi: 10.1016/j.jmmm.2011.09.037

de Vries J, Bolhuis T, Abelmann L, 2013
"Energy barrier versus switching field for patterned $Co_{80}Pt_{20}$ alloy and Co/Pt multilayer films"
J. Appl. Phys. **113**, pp. 17B910–1–17B910–3, doi: 10.1063/1.4801399

Three more publications are in preparation: an article based on chapter 3 on the results of the statistical measurements, an article based on chapter 4 on the low temperature measurements and an article based on chapter 5 on the mega- to gigayear data storage medium.

Conference contributions

Keuning J D, de Vries J, Abelmann L, Misra S, 25-30 Sept 2011
"Image-based magnetic control of paramagnetic microparticles in water"
In: *Proc. IEEE/RSJ International Conference on Intelligent Robots and Systems*, San Francisco, CA, USA.

de Vries J, Abelmann L, Manz A, Elwenspoek M, 26-29 Sept 2010
"Tungsten-siliconnitride medium for mega- to gigayear data storage"
In: *Proc. Micromechanics and Microsystems Europe*, Enschede, The Netherlands

de Vries J, Delalande M, Abelmann L, Alexandrou M, Schedin F, Nutter P, Hill E, Thomson T, 12-16 July 2010
"Simulation of position sensitivity of the anomalous Hall effect on a single magnetic dot"
In: *Proc. International Symposium on Advanced Magnetic Materials and Applications*, Sendai, Japan

de Vries J, Delalande M Y, Abelmann L, Lodder J C, 7-11 May 2011
"Measurement of the nucleation and propagation field in a single Co/Pt multilayer dot by anomalous Hall effect"
In: *Proc. IEEE International Magnetics Conference*, Taipei, Taiwan

de Vries J, Keuning J, Zondervan L, Misra S, Abelmann L, 19-22 June 2011
"Image-based magnetic control of self-propelling catalytic micro motors"
In: *Proc. Micromechanics and Microsystems Europe*, Tonsberg, Norway

de Vries J, Abelmann L, Manz A, Elwenspoek M C, 9-12 Sept 2012
"Tungsten-siliconnitride medium for Mega- to Gigayear data storage"
In: *Proc. Micromechanics and Microsystems Europe*, Ilmenau, Germany

de Vries J, Bolhuis T, Wolferen van H A G M, Siekman M H, Abelmann L, 7-11 May 2012
"Thermally induced switching field distribution of sub-micron CoPt alloy and Co/Pt multilayer islands"
In: *Proc. IEEE International Magnetics Conference*, Vancouver, Canada

de Vries J, Bolhuis T, Abelmann L, 14-18 Jan 2013
"Energy barrier versus switching field for patterned $Co_{80}Pt_{20}$ alloy and Co/Pt multilayer films"
In: *Proc. Joint MMM/IEEE International Magnetics Conference*, Chicago, Il, USA

Biography

Jeroen de Vries was born on the 5th of January 1982 in Stede Broec. He attended primary school in Grootebroek and went to the St. Martinuscollege in Grootebroek, to obtain the VWO diploma. In 2000 he moved to Enschede to study electrical engineering. From December 2007 until April 2008 he stayed in Akita, Japan at the group of Prof. Hitoshi Saito at Akita University for an internship investigating the theoretical sensitivity of cantilever tip shapes. He continued with an assignment investigating optical readout of parallel cantilever arrays at the Systems and Materials for Information storage (SMI) group. He graduated in 2009 after which he started his PhD research at the Transducers Science and Technology (TST) group, which is described in this thesis. During his PhD research he attended the IEEE summer school on magnetism in Dresden, Germany and the ESONN summer school on nanotechnology in Grenoble, France.

Biografie

Jeroen de Vries werd geboren op 5 januari 1982 in Stede Broec. Hij ging naar de basisschool in Grootebroek en vervolgens naar het St. Martinuscollege om het VWO diploma te behalen. In 2000 verhuisde hij naar Enschede om elektrotechniek te studeren. Van december 2007 tot april 2008 verbleef hij in Akita, Japan bij de groep van Prof. Hitoshi Saito aan de Akita universiteit om de theoretische gevoeligheid van cantilever tip vormen te bestuderen. Hij vervolgde met een onderzoek naar het optisch uitlezen van een cantilever array bij de Systems and Materials for Information storage (SMI) groep. Hij studeerde af in 2009 waarna hij begon als promovendus bij de Transducers Science and Technology (TST) groep, waarvan het onderzoek beschreven is in dit proefschrift. Tijdens zijn promotieonderzoek nam hij deel aan de IEEE summer school on magnetism in Dresden, Duitsland en de ESONN summer school over nanotechnologie in Grenoble, Frankrijk.

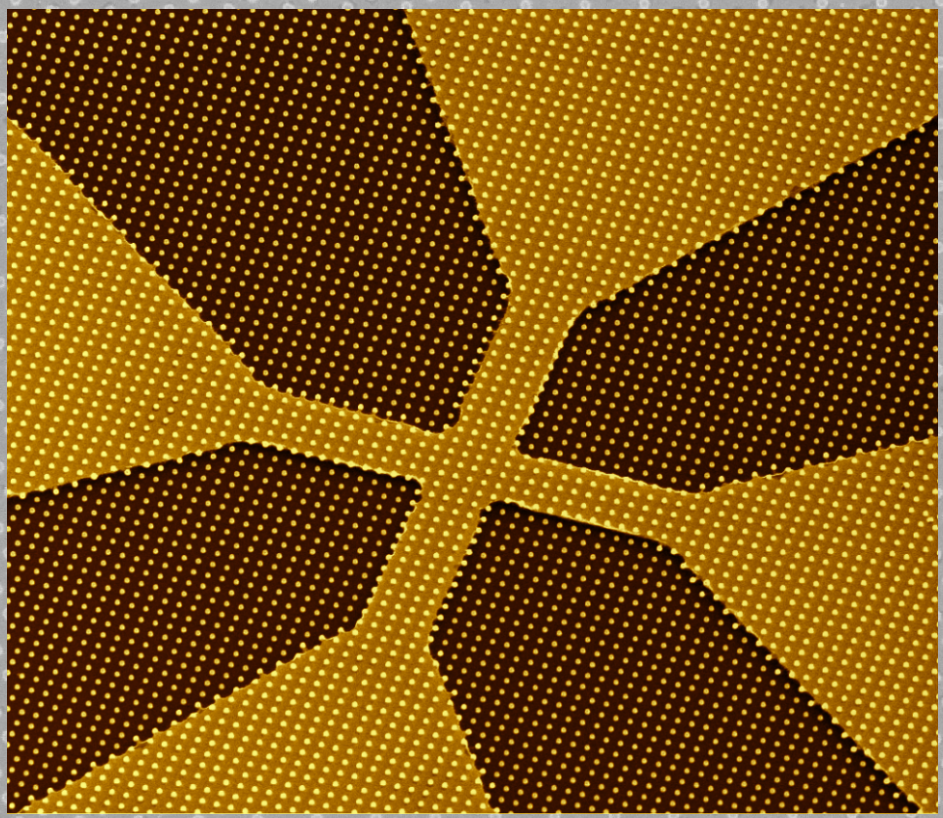

ISBN 978-90-365-0640-3